

Dynamics and Predictability of Hurricane Humberto (2007)
Revealed from Ensemble Analysis and Forecasting

Jason A. Sippel

NASA's Goddard Space Flight Center, Greenbelt, Maryland

Fuqing Zhang

Department of Meteorology, The Pennsylvania State University, University Park, Pennsylvania

Submitted to *Journal of the Atmospheric Sciences* for Publication

March 10, 2009

Corresponding author address: Dr. Jason A. Sippel, NASA GSFC, Code 613.1, Greenbelt, MD
20771. Email: sippel@agnes.gsfc.nasa.gov

Abstract

This study uses short-range ensemble forecasts initialized with an Ensemble-Kalman filter to study the dynamics and predictability of Hurricane Humberto, which made landfall along the Texas coast in 2007. Statistical correlation is used to determine why some ensemble members strengthen the incipient low into a hurricane and others do not. It is found that deep moisture and high convective available potential energy (CAPE) are two of the most important factors for the genesis of Humberto. Variations in CAPE result in as much difference (ensemble spread) in the final hurricane intensity as do variations in deep moisture. CAPE differences here are related to the interaction between the cyclone and a nearby front, which tends to stabilize the lower troposphere in the vicinity of the circulation center. This subsequently weakens convection and slows genesis. Eventually the wind-induced surface heat exchange mechanism and differences in landfall time result in even larger ensemble spread.

1. Introduction

Understanding the source of uncertainty in tropical cyclone intensity forecasts continues to be a significant concern, especially given the recent lack of improvement in intensity forecasts (e.g., Franklin 2005; Elsberry et al. 2007). Predictions of tropical cyclone formation, rapid intensification and decay remain particularly problematic (Houze et al 2007), yet our knowledge of how error grows in such forecasts remains very limited (Van Sang et al. 2008). A better understanding of this problem can potentially lead to improved forecasts and is the motivation of the current study.

Sippel and Zhang (2008) (hereafter SZ08) and Zhang and Sippel (2009) (hereafter ZS09) used mesoscale ensembles and sensitivity studies to elucidate the source of tropical cyclone intensity forecast uncertainty. SZ08 found that variations in convective available potential energy (CAPE) and deep moisture were two factors that strongly influenced genesis in forecasts of a non-developing Gulf of Mexico low. Ensemble members with higher initial values of these two variables had heavier subsequent precipitation, which caused their cyclones to strengthen more quickly. The resulting intensity differences between cyclones in different ensemble members were exaggerated by differences in oceanic heat fluxes and eventually by differences in the extent to which the WISHE process activated [e.g., Emanuel (1986), Rotunno and Emanuel (1987), and Emanuel et al. (1994)]. Meanwhile, ZS09 investigated the same low and found that differences in initial conditions much smaller than current observation and analysis error can cause very strong differences in convection and ultimately determine whether or not a tropical cyclone forms. The strong sensitivity of precipitation (and thus cyclone strength) to small changes in initial conditions observed in SZ08 and ZS09 is consistent with previous findings

regarding the negative influence of moist convection on atmospheric predictability (Islam et al. 1993; Olson et al. 1995; Zhang et al. 2002, 2003, 2006, 2007; Zhang 2005; Bei and Zhang 2007).

This study is intended as a follow-up to test the results of SZ08 and ZS09. One of their results that warrants particular attention regards the role of CAPE in tropical cyclone formation. Generally speaking, CAPE is not believed to be a significant factor in tropical cyclone genesis and intensification, especially compared to mid-level moisture, shear, sea-surface temperature, and pre-existing vorticity (E. Zipser 2009, personal communication). The recent study of Nolan et al. (2007) concurred with that sentiment, finding that there is *no* relationship between CAPE and the rate of cyclogenesis in an otherwise favorable environment. Some studies, such as Kerns and Zipser (2009) have elected not to use atmospheric stability to statistically discriminate developing from non-developing tropical disturbances. This practice is based partly on the observational finding that the *areal extent* of convection is a better predictor of future tropical cyclone strength than the *intensity* of convection (e.g., Cecil and Zipser 1999). Yet, the modeling study of Montgomery et al. (2006) hypothesized that CAPE plays a role in the intensification of vortical hot towers (VHTs), which are known to help build the tropical cyclone vortex (Hendricks et al. 2004). Also, in 2003 a crude representation of atmospheric stability was *added* to the operational SHIPS model, which makes statistical-dynamical predictions of hurricane intensity (DeMaria et al. 2005). Thus, some clarification is needed to elucidate the extent to which CAPE hastens tropical cyclone formation.

The research presented here uses an ensemble forecast from the Weather Research and Forecasting (WRF) model initialized with an ensemble Kalman filter analysis of WSR-88D radar observations [see Zhang et al. 2009 (hereafter Z09)] to investigate the probabilistic dynamics and

predictability of Hurricane Humberto, which made landfall on the upper Texas coast in 2007. Data and methodology are described in section 2, and an overview of the genesis environment is presented in section 3. Section 4 examines the ensemble performance and predictability of the event while section 5 presents the probabilistic dynamics. A summary and discussion are presented in section 6.

2. Data and methodology

This investigation employs methodology originally developed in Zhang (2005) and Hawblitzel et al. (2007) and refined in SZ08 by investigating probabilistic dynamics using an ensemble forecast. A similar method has also been used by Hakim and Torn (2008) to study the dynamics of mid-latitude cyclones.

2.1 Forecast model and data assimilation methods

The EnKF-WRF analyses and ensemble forecasts of Z09 are used here, and a brief synopsis of the setup follows. The outer, 40.5-km WRF domain covers the contiguous United States with 160×121 grid points and two nested domains cover the south-central United States and north Gulf of Mexico with 160×121 (253×253) grid points and a grid spacing of 13.5 (4.5) km (see Fig. 2 of Z09). All model domains have 35 vertical layers, and the model top is set at 10 hPa. Random, balanced, large-scale perturbations are added to the National Centers for Environmental Prediction (NCEP) Global Forecast System (GFS) analyses at 0000 UTC 12 September to create initial conditions for a 30-member ensemble forecast that is integrated forward until 0900 UTC. Data assimilation of thinned and quality controlled radial velocity observations from the Corpus Christi (KCRP) and Houston-Galveston (KHGX) radars begins at

0900 UTC. Assimilation proceeds in hourly cycles until 1800 UTC 12 September, at which point an EnKF-initialized ensemble forecast is integrated forward. See Z09 for details on the EnKF and WRF setup and performance.

The use of an EnKF for the analyses here is a significant difference from the methodology of SZ08. In the analysis of SZ08, a cold-start technique was used, which possibly resulted in some artificial overreaction of initial convection to ambient convective instability during the model spin-up period. For example, precipitation totals in SZ08 were generally considerably higher during the first 12 h than at later times, especially for those members with higher CAPE and/or mid-level moisture (e.g., their Fig. 12). This same trend was noted in the sensitivity study of ZS09 (e.g., their Fig. 7). The possibility that model spinup affected the results in SZ08 and ZS09 is further motivation for the current work, in which the so-called “hot-start” EnKF analyses contains active moist convection (see Fig. 1). As will be seen later, the difference in techniques *does* have some effects on results.

2.2 Correlation and probabilistic dynamics

As in SZ08, linear correlation is used here to elucidate dynamics, but verbal descriptions of correlation will be somewhat different than in that study. Since the size of the ensemble used here is larger (i.e., 30 vs. 20 members), confidence that a particular level of correlation is statistically different from 0 is higher here. This paper continues using the SZ08 correlation benchmarks of 0.3, 0.5, and 0.7, and here these values are significant with roughly 90%, 99.5%, and 99.99% confidence, respectively. Verbal descriptions of the correlation values will respectively be ‘significantly correlated’, ‘strongly correlated’, and ‘very strongly correlated’.

Also as in SZ08, statistical control is sometimes used to elucidate the correlation between two variables while effectively holding a third variable constant. For example, if variables A , B , and C are all correlated, then $(A:B)$ is the correlation between A and B , and $(A:B|C)$ is the correlation between A and B when controlling for C . The controlled correlation is calculated by removing the variation in B that results from its relationship with C . In other words, linear regression between B and C is first used to predict values of B given C , and the residuals between the actual and predicted values of B are then calculated. Finally, A is correlated to the residuals to compute the controlled correlation $(A:B|C)$. As applied here, A is the field being tested for sensitivity, C is a measure of storm intensity at the time of A , and B is a measure of intensity at a later time. Using this methodology thus helps to determine the extent to which variation in A influences the intensification of a storm of a given intensity.

Investigating which variables early in the genesis phase are well correlated with the intensity of the mature cyclone is useful because it reveals the factors that favor intensification and increase ensemble spread. Abiding by the SZ08 convention, here we define the intensity metric $SLPf$, which is area-average SLP within 20 km of the cyclone center 0600 UTC 13 September. This time is useful because it is before most ensemble members make landfall, though the results are very similar with a slightly later time when the mean strength is higher but more ensemble members have storms that have made landfall. The 20-km radius was chosen largely because it produces $SLPf$ that exhibits the best time-lag correlation with SLP averaged over the same area at other earlier times (hereafter $SLPt$). For example, Figure 2 shows a scatterplot of $SLPt$ at 1800 UTC 12 September versus $SLPf$, the linear best-fit, and the correlation between the two variables. The correlation, which is nearly 0.9, demonstrates the

very strong time-lag relationship. Finally, as in SZ08 the negative of SLP_t and SLP_f will be used in correlation computations so that positive correlation with SLP_f implies that a factor favors intensification.

3. Synoptic overview and genesis environment

Hurricane Humberto rapidly formed off the upper Texas coast on the morning of September 12, 2007 (Fig. 3c). The system was operationally declared a tropical depression at 1500 UTC, though the best-track post-event analysis issued by the NHC estimates that the depression had formed by 0900 UTC and that the system was a 17.5-m s^{-1} tropical storm by 1200 UTC (Fig. 3b). By the time of its landfall east of High Island, TX at 0700 UTC 13 September, the storm had strengthened to a 40-m s^{-1} , Category 1 hurricane. Thus, the cyclone intensified by approximately 22.5-m s^{-1} in the 19 hours before its landfall, which makes it the most rapidly intensifying, near-landfall storm in US records.

The initial local environment preceding the development of Hurricane Humberto was relatively favorable for genesis, although unfavorable factors lingered on a larger scale. The focus for convection prior to cyclogenesis was an inverted trough at low- to mid-levels that manifested itself at the surface as a weak low (Fig. 4). This system had moved westward across the Gulf of Mexico during the preceding week, and the NHC recognized it as a potential trigger for cyclogenesis as early as the afternoon of 10 September. Convection associated with the disturbance had access to modest convective instability (Fig. 4c), and it gradually became more widespread and organized preceding Humberto's genesis (Fig. 1). In addition, by 0900 UTC 12 September the *local* genesis environment was rich with deep moisture (Fig. 4a,b), which is a

necessary genesis ingredient according to Rotunno and Emanuel (1987) and Emanuel (1989). Yet, on a larger scale in Fig. 4a-b, significantly drier and more stable air associated with a frontal boundary was not far north of the developing cyclone and could certainly hinder genesis if it entrained into the circulation. Additional drier pockets at 700 hPa were also evident farther south over the Gulf of Mexico, and they too could potentially hinder genesis. Finally, the ample convection in the genesis region likely helped reduce upper level PV and build an upper level ridge above the circulation center (Fig. 4d). Associated with the ridge was a minimum in the 200-850-hPa shear. Mean shear within 300 km of the circulation center on 12 September was well below 12.5 m s^{-1} (Fig. 5a), which is favorable for intensification according to DeMaria et al. (2001).

Humberto's development and evolution posed serious operational forecast challenges. All operational models failed to capture the storm's rapid genesis and deepening to a formidable Category 1 hurricane. For example, Z09 demonstrated the severity of the failure of multiple real-time forecasts by the operational global forecast system (GFS) running at National Centers for Environmental Prediction (NCEP). They also showed that the WRF model failed in post-event, 4.5-km, cloud-resolving simulations that were initialized with GFS analyses with lead times every 6 h from 6 to 48 h.

The failure of all operational models to capture the rapid intensification of Humberto led to significant operational intensity forecast errors. First, while tropical weather outlooks issued by the NHC mentioned the preceding disturbance for several days prior to genesis, none mentioned the possibility that depression formation was imminent. Also, though the official track errors were less than long-term average track error, average 12-h intensity forecast error was

300% of long-term average intensity error with the same lead-time. This failure highlights the current struggle to forecast rapid intensity change of tropical cyclones in general.

4. Ensemble performance and predictability

Z09 found that use of an EnKF could significantly benefit the prediction of Humberto. In particular, assimilation of radial velocity observations from three WSR-88D radars along the gulf coast resulted in analyses that accurately depicted the best-track position and intensity of Humberto. In addition, EnKF-initialized deterministic (not shown) and ensemble (Fig. 3) forecasts outperformed operational forecasts by predicting the rapid formation and intensification of the hurricane.

Not only does the current ensemble capture the genesis and rapid intensification of Humberto, but also forecasts from some individual members also reasonably depict Humberto's structure. To further demonstrate this, Figure 6 shows observed reflectivity from the time around Humberto's landfall and derived reflectivity at the landfall time of ensemble members 1, 16 and 19 (these members generally span the ensemble in terms of *SLPf* in Fig. 2). Of the three members shown, member 1 (Fig. 6b) best represents the central structure of Humberto with a well-organized central core and a 50% closed eyewall. In terms of minimum SLP, it is somewhat weaker than Humberto at its landfall, but other storms in the ensemble do obtain lower central pressure (see Fig. 3a). One noticeable problem with the storm in member 1 and other strongly developing ensemble members in Fig. 3 is that they strengthen the storm too slowly. Humberto's actual central pressure falls below the lower limit of the ensemble envelope until its landfall, after which many ensemble members obtain a similar central pressure to the lowest

observed with the storm. Aside from member 1, member 16 (Fig. 6c) does a mediocre job at representing Humberto's intensity and structure, and member 19 (Fig. 6d) does a poor job. Yet, both members perform better than did the operational models.

In addition, certain members also accurately demonstrate the storm's interaction with a nearby surface front. For instance, Fig. 7a shows a mesoscale analysis of Humberto shortly before the hurricane made landfall, and Fig. 7b shows the corresponding member 1 forecast for 1500 UTC 13 September, shortly after the cyclone in that member makes landfall. The observations in Fig. 7a reveal that Humberto's circulation had begun entraining cool post-frontal air before landfall, which might explain the observed lack of convection on the southwest side of the storm (e.g., Fig. 6a). The forecast temperature field in Fig. 7b exhibits a very similar wavelike pattern to that observed in Fig. 7a, and the temperature difference across the front is about the same in both panels. In addition, the simulated storm similarly lacks convection on its southwest side (Fig. 6b). Finally, a wavelike field seen in both dew-point observations and the simulation (not shown) indicates that the air entraining into the circulation from the northwest was also drier than that of its immediate genesis environment.

The ensemble captures Humberto's general track, but it moves the storm northeastward too slowly. For example, in Fig. 3c the actual position of the cyclone at 1200 UTC 13 September is well northeast of all the ensemble members. This error is partly a result of the left track deviation that takes place after 1800 UTC 12 September (i.e., after the final EnKF analysis) in many of the ensemble members. One result of this error is that many members make landfall 6-12 h later than did Humberto, which is evident by the late end of their intensification cycles in Fig. 3a-b.

Despite the benefits of data assimilation, the very large ensemble intensity spread in Fig. 3a-b exemplifies the significant uncertainty associated with the intensity forecast of Hurricane Humberto. In fact, ensemble spread grows much more rapidly in the case of Humberto than in the 2004 gulf low studied in SZ08. For instance, the minimum SLP envelope here spans nearly 30 hPa after 18 h of forecast time (i.e, by 1200 UTC 13 September in Fig. 3a), but the envelope in the gulf low was only 14 hPa after 36 h (when sampled on their 3.3-km grid, see Fig. 3 of ZS09). As a result of the larger intensity spread in the Humberto case, RM-DTE error grows much faster. In Fig. 8, RM-DTE¹ increases from about 3 m s⁻¹ at 1800 UTC 12 September to over 10 m s⁻¹ by 1200 UTC 13 September (to facilitate comparison to SZ08, RM-DTE has been sampled every 7 grid points, or 31.5 km, in Fig. 8). This >300% RM-DTE increase occurs in only half the time of a similar percentage increase in ZS08 (see their Fig. 5). Thus, forecast uncertainty was considerably higher with Humberto than with the 2004 low. Ultimately, the presence of extreme spread with the relatively accurate ensemble-mean performance renders this an excellent case with which to test the results of SZ08.

The strong deviation of some ensemble members from the best-fit line in Fig. 2 further highlights the lack of predictability in this case. In particular, the strongest member at 0600 UTC 13 September starts out with nearly identical SLP to several other members at 1800 UTC 12 September that develop into much weaker storms. This large change in intensity due to a very small change in initial conditions is reminiscent of the results of ZS09. Moreover, the three strongest members at 0600 UTC 13 September also do not closely follow the mean dynamics.

¹ The root-mean of difference total energy (RM-DTE), where difference total energy (DTE) is defined as $DTE = 0.5(u'u' + v'v' + kT'T')$ and $k = C_p / T_r$ ($C_p = 1004.9 \text{ J kg}^{-1} \text{ K}^{-1}$ and $T_r = 270 \text{ K}$). See SZ08 for more details.

They are weaker than a number of the other members at 1800 UTC 12 September, but they subsequently intensify more quickly than the other strong members. Though sensitivity to initial conditions among the subset of strong members is interesting, the remainder of this study focuses on the mean dynamics represented by the overall correlation among all ensemble members.

5. Probabilistic dynamics

This section divides the dynamical examination into two time periods; one is from 0900 to 1800 UTC 12 September, and the other is after 1800 UTC. The first reason for doing this is that SLP at 1800 UTC largely explains $SLPf$ variance (Fig. 2), but spread increases tremendously *after* 1800 UTC (Figs. 3 and 8). Thus, processes acting before 1800 UTC explain most of final differences between ensemble members, and whatever happens later only acts to increase spread while maintaining the same correlation statistics. A second reason for dividing the analysis into two periods is that 1800 UTC is the starting time for the pure ensemble forecast. Thus, the division also shows how spread increases during the EnKF analysis/forecast cycles and the means by which post-1800 UTC spread increases during the pure ensemble forecast period.

5.1 Early convection and details of PV tower building

To elucidate the pre-1800 UTC intensification process, we focus on the low-level PV since it is known to be a reliable indicator of tropical cyclone intensity. For the purposes of this study, the average PV at 2 km within the ensemble-mean 2-PVU isopleth (see Fig. 9 for the isopleths) is used to represent the intensity of the incipient low-level vortex before 1800 UTC. Meanwhile, we use the average 1-h precipitation within the ensemble-mean 10-mm isopleth (see Fig. 9 for these isopleths; hereafter referred to *PTOT*) to represent the strength of early deep

convection since it is known to intensify the tropical cyclone vortex. The correlation between $SLPf$ and both PV ($PV:SLPf$) and $PTOT$ ($PTOT:SLPf$) is shown in Fig. 5b. To better illustrate the *causal* role of convection in intensification, Fig. 5 also shows the correlation between $PTOT$ and both PV and $SLPf$ when controlling for cyclone strength in terms of PV at the beginning of each precipitation period (PV_{t-1}).

Deep convection during the assimilation period before 1800 UTC builds low-level PV, which results in lower $SLPf$. The strong convection that develops near the circulation center subsequent to the 1000-UTC analysis (Fig. 9b) dramatically increases ($PTOT:SLPf$), ($PTOT:SLPf|PV_{t-1}$), and ($PTOT:PV|PV_{t-1}$). The controlled correlation between $PTOT$ and PV at 1100 and 1200 UTC is significant to strong, which is consistent with the knowledge that deep convection tends to increase low-level PV (Haynes and McIntyre 1987). Likewise, a low-level PV anomaly develops amidst the deep convection in the ensemble mean (Fig. 9b-c). By around 1300 UTC, nearly all convection diminishes (Fig. 9d-e), and the lack of ($PTOT:SLPf$) at 1400 UTC in Fig. 5b results from the lack of a 10-mm isopleths (this demonstrates the intermittency of deep convection at early times). By 1500 UTC, convection begins again in earnest (Fig. 9f-g), and after 1500 UTC ($PTOT:SLPf$) is again significantly positive. Meanwhile, the 1600-UTC controlled correlation ($PTOT:SLPf|PV_{t-1}$) shows that heavier precipitation between 1500 and 1600 UTC has a direct impact on $SLPf$. Thus, variance in precipitation in deep convective regions before 1800 UTC 12 September is a significant source of $SLPf$ variance.

Correlation between PV and $SLPf$ increases steadily through the morning of 12 September, and it becomes very strong as new convection erupts and the low-level PV anomaly dramatically intensifies. In the ensemble mean, the PV tower at the cyclone center is a result of

the merger between two PV anomalies that originate in active convection between 1000 and 1100 UTC (Fig. 9a-f). The convection diminishes after 1200 UTC, and the anomalies strengthen very slowly until the merger at 1500 UTC. Around the time of the merger, convection begins again, and the newly formed PV tower begins to rapidly strengthen (Fig. 9f-i). By 1600 UTC, correlation between PV inside the 2-PVU isopleth (hereafter *PV16Z*) and *SLPf* is 0.87; this means that 75% of *SLPf* variance can be explained by variance of *PV16Z*.

Aside from convection, another source of PV variance is likely the data assimilation process. For example, data assimilation apparently increases low-level PV in the absence of ensemble convection between 1200 and 1400 UTC (not shown), and it likely continues to do so as ensemble convection commences. The extent to which data assimilation acts independent of ensemble dynamics to increase PV spread is beyond the scope of this study.

Figure 10 demonstrates how the above results relate to individual ensemble members highlighted in Fig. 2 and how those members evolve through 1800 UTC. All the members shown have multiple low-level PV anomalies with scales between 5 and 30 km at 1600 UTC (similar results are also seen at earlier times). These anomalies, which resemble the VHTs introduced by Hendricks et al. (2004) and Montgomery et al (2006), occur in both isolated areas and in clusters. The clusters are similar to the clusters of VHTs noted in ZS09 and might be akin to the convective burst vortices observed in Sippel et al. (2006). In general, the members with stronger and more widespread convection have stronger and larger PV anomalies. For example, member 1 (Fig. 10a-c) has very strong precipitation maxima directly upstream of its strong PV maxima at 1600 UTC. The PV subsequently becomes associated with the circulation center, giving member 1 the strongest near-center PV at 1800 UTC (Fig. 10c). Meanwhile, though

member 16 (Fig. 10d-f) has fairly intense convection and maximum PV strength about the same as that in member 1, its convection and strong PV are less widespread. Finally, the storm in member 19 (10g-i) has the least convection and PV at 1600 UTC, and it remains the weakest, least organized storm.

The differences in low-level PV organization at 1800 UTC are associated with varying intensities in terms of SLP and surface winds. For example, the cyclone in member 1 is strongest in terms of minimum SLP and maximum surface winds (Fig. 11a), which are local-scale strength metrics used in the operational environment. The member-1 cyclone is also strongest in terms of area-average metrics in Fig. 11b, which are less sensitive to very small-scale variations and are more consistent indicators of strength from one time to the next (e.g., ZS09). These characteristics are consistent with the strong PV core in that member. Member 16 generally has less core PV strength and organization than member 1 at 1800 UTC, and its SLP and winds are weaker than those in member 1. Finally, the unorganized PV core in member 19 yields the weakest surface winds and highest central pressure.

To summarize, it was shown in this subsection that strength of the low-level PV anomaly by 1600 UTC 12 September strongly controls the ultimate strength of the cyclone. This anomaly results from the merger of two smaller anomalies, and its magnitude is modulated by the strength of the earlier PV field, the amount of precipitation that falls during an eruption of convection around 1500 UTC, and probably by the data assimilation process itself. The intensity of the smaller anomalies is also related to the same three factors. The next several subsections will analyze what specific initial factors both favor and inhibit ensemble convection on the morning of 12 September.

5.2 Contributors to precipitation: MUCAPE and deep moisture

SZ08 found that both deep moisture and CAPE were beneficial for the development of a 2004 Gulf of Mexico surface low into a tropical cyclone. When the magnitude of either moisture or CAPE increased, more convection resulted, and a stronger cyclone formed. Thus, this section investigates how these factors affect convection at the times when convection is found to be an independent positive contributor to cyclone intensification (e.g., from 1000 to 1200 UTC and from 1500 to 1600 UTC).

The amount of precipitation that develops near the circulation center between 1000 and 1200 UTC in Fig. 9b-c is strongly related to the ambient convective instability. To demonstrate this, Figure 12 shows ensemble-mean, 1-h precipitation valid at 1100 and 1200 UTC 12 September along with the correlation between $PTOT$ and MUCAPE² 1 hour before the precipitation period begins. Precipitation at both times is significantly to strongly correlated with preceding MUCAPE. In addition, the pattern of correlation between $PTOT$ and surface temperature (hereafter T_{sfc}) is very similar to that shown in Fig. 12 (not shown). Combined, these results suggest that an increase in T_{sfc} leads to an increase in MUCAPE, which results in more precipitation and production of a stronger PV anomaly (e.g., Fig. 5). Finally, higher amounts of mid-level moisture do not contribute to higher $PTOT$ at 1100 and 1200 UTC (not shown).

Higher T_{sfc} and MUCAPE also contribute to precipitation and cyclone intensification between 1500 and 1600 UTC. To show this, ensemble-mean T_{sfc} (MUCAPE) is overlain with

² MUCAPE is computed as the CAPE for the parcel in each column with maximum equivalent potential temperature within the lowest 3000 m. Following the recommendation of Doswell and Rasmussen (1994), virtual potential temperature is used in this calculation.

the correlation between $PTOT16Z$ and $Tsfc$ (MUCAPE) in Fig. 13a,d (Fig. 13b,e). At this time, precipitation that contributes to $PTOT16Z$ falls generally downstream of distinct ensemble-mean MUCAPE maxima where MUCAPE is significantly correlated with $PTOT16Z$ (Fig. 13b,e). As before, $(Tsfc:PTOT16Z)$ is similar to $(MUCAPE:PTOT16Z)$, and surface temperatures upstream of the $PTOT16Z$ region are quite clearly beneficial to convection within the $PTOT16Z$ boundary. In a specific example, member 19 has the coolest surface air immediately southwest of the circulation center (i.e., upstream of $PTOT16Z$ convection, see Fig. 14c) and generally less precipitation in the $PTOT16Z$ region than members 1 or 16 (Fig. 14a,b). Both $(Tsfc:SLPf)$ and $(MUCAPE:SLPf)$ are respectively quite similar to $(Tsfc:PTOT16Z)$ and $(MUCAPE:PTOT16Z)$, which shows that the variance in $Tsfc$ and MUCAPE that leads to precipitation differences also leads to similar differences in $SLPf$ (not shown).

Mid-level moisture also benefits precipitation intensity between 1500 and 1600 UTC. Figure 13c,f shows ensemble-mean mid-level (3-6 km average) moisture (hereafter, $qmid$) and its correlation with $PTOT16Z$ ($qmid:PTOT16Z$). The large meridional band of strong correlation in Fig. 13c,f indicates that more precipitation falls when preceding mid-level moisture is higher. Though some $qmid$ variance in an area southeast of the circulation center is related to precipitation totals between 1000 and 1200 UTC (not shown), moisture in most of the region is unaffected by the earlier convection. Thus, $(qmid:PTOT16Z)$ illustrates a direct causal role that mid-level moisture has in enhancing precipitation and thus genesis.

5.3 Frontal interaction: An inhibiting factor

Interaction with the front directly limits intensification in some ensemble members. Figure 15, which shows ensemble-mean surface mixing ratio (hereafter $qsfc$) and $Tsfc$ along with

($qsfc:SLPf$) and ($Tsfc:SLPf$) at 0900 UTC 12 September, clearly demonstrates that the front negatively impacts $SLPf$ (the approximate position of the front is shown with a white line along the 298-K isotherm and 17- $g\ kg^{-1}$ isodrosotherm). Strong ($qsfc:SLPf$) and ($Tsfc:SLPf$) to the north of the boundary indicate that a weaker front is more favorable for cyclogenesis, and similar correlation patterns at later times (not shown) indicate that the front continues to negatively impact cyclogenesis through the afternoon hours of 12 September. Figure 14 reveals the negative influence of the front very early in some ensemble members. Members 16 and 19, which have weaker cyclones than those in member 1, have cooler air behind the front and also tend to ingest post-frontal air sooner. This is demonstrated by differences in location of the 299-K isotherm in Fig. 14 and is partially a cause of the strong correlation between $PTOT16Z$ and $Tsfc$ in Fig. 13a,d. In fact, the region of significant to strong ($PTOT16Z:Tsfc$) in Fig. 13a,d originates over land, north of the front several hours earlier (not shown) and moves south to its observed position in Fig. 13a. Since previous subsections show that convection leading to genesis is weaker when surface temperatures and instability are lower, the effect of the front is to diminish this convection and ultimately limit PV production and genesis.

5.4 Post-1800 UTC evolution

To review, it was previously shown that variance in storm intensity by 1800 UTC explains a vast majority of $SLPf$ variance. Stronger storms at 1800 UTC evolve from stronger low-level PV anomalies that initially appear around 1100 UTC in the ensemble mean. These anomalies are built by intense convection, which itself is fed by higher MUCAPE and mid-level moisture. Since a stronger surface front reduces surface temperature and convective instability in the genesis region, it also inhibits genesis. Finally, since $SLPf$ is so strongly correlated with

1800-UTC cyclone strength, any processes acting after 1800 UTC generally only increase existing differences. This subsection investigates how spread increases after 1800 UTC.

Interaction with the surface front continues to be an important mechanism governing cyclone intensity through 0000 UTC 13 September, and the storm's track becomes an increasingly important factor in determining the extent of cyclone-front interaction. At and before 1800 UTC, track spread is fairly low because EnKF analyses adjust the cyclone position in all members toward the observed track. Therefore, differences in storm position before 1800 UTC probably do not significantly determine the extent of pre-1800-UTC cyclone-front interaction. However, position spread increases substantially after 1800 UTC, when the background wind is free to advect cyclones without track adjustment by the filter. Ensemble members with a stronger westerly wind component have cyclones move northeast (e.g. member 1 in Fig. 3d), somewhat parallel to the front, while members with a stronger easterly component have storms that move northwest toward the front (e.g. member 19 in Fig. 3d). The 2100-UTC result of larger track spread is a much stronger track-dependent difference in cyclone-front interaction. This is demonstrated in Fig. 16, where members 16 (Fig. 16b) and 19 (Fig. 16c) have cyclones that are visibly further west and closer to the front than that in member 1 (Fig. 16a). Also, for an undetermined reason, the regional westerly wind component below 6 km is strongly anticorrelated to front strength (not shown). Thus, since low- to mid-level winds control the track of tropical cyclones, ensemble members with stronger fronts also have cyclones that take a more westerly course. For example, note the dryer air behind the front in members 16 and 19 (Fig. 16b-c), and recall their track and position relative to the front. Ultimately, storms

embedded in weaker westerlies (stronger easterlies) face a serious uphill battle because they must fight a stronger front *in addition to* encountering the front sooner.

Concomitant with the presence of the front, convective instability also continues to be an important intensification factor. To demonstrate the effect of cyclone-scale MUCAPE changes on intensification, Fig. 17a shows the evolution of azimuthally averaged MUCAPE and its correlation with $SLPf$ when controlling for $SLPt$. MUCAPE within 60 km of the circulation center remains a strong influence on $SLPf$ as the coverage and intensity of diabatic heating increases (e.g., Fig. 17c). Figure 18, which shows correlation between $Tsfc$ and average precipitation within heavier precipitation regions (i.e., in the gray boxes) demonstrates the above on local scales. As is the case earlier in the day, mean precipitation is very sensitive to its inflow temperature (or instability). Thus, stronger instability results in stronger and/or more widespread convection, which itself leads to a stronger storm (e.g., Fig. 17c).

Interestingly, MUCAPE variance appears to result in at least as much cyclone strength spread as does $qmid$ variance. For example, Fig. 17b shows the correlation between $qmid$ and $SLPf$ when controlling for $SLPt$. The area of significant correlation, which is only over the immediate center, is much smaller than the area of MUCAPE correlation. This result is somewhat different than the control simulation of SZ08, where the importance of CAPE on the larger scale was secondary to that of mid-level moisture. Cyclone-scale mid-level moisture in the current study is probably sufficient for genesis in most ensemble members, whereas that is not necessarily the case for CAPE. Perhaps the relative difference in correlation is not surprising considering that control simulation of SZ08 had initial MUCAPE of approximately 1700 J kg^{-1} , whereas here it is significantly less than 1000 J kg^{-1} until 0000 UTC 13 September. Thus, it

appears that CAPE is sufficiently low in the present case that its variation can strongly modify mean diabatic heating and the rate of genesis.

The WISHE mechanism, which SZ08 showed to amplify ensemble spread even further, becomes increasingly dominant from late 12 to early 13 September. One strong indication of the onset of WISHE is the cessation of widespread cold convective downdrafts (Rotunno and Emanuel 1987; Emanuel 1989), which are prevalent through much of 12 September. For instance, surface temperatures downstream of the boxed area in Fig. 18a are strongly anticorrelated to mean precipitation within the boxed region. In addition, even precipitation near the cyclone center produces downstream cold pools through 0000 UTC 13 September (Fig. 18b). However, after 0000 UTC anticorrelation between T_{sfc} and convection ceases to be statistically significant immediately surrounding the cyclone center (Fig. 18c). Thus, it appears that WISHE might be fully active after 0000 UTC 13 September.

Other changes also signal the onset of WISHE and mature tropical cyclone dynamics. For example, oceanic heat fluxes (hereafter used interchangeably with FLUX) increase steadily until 0000 UTC 13 September (Fig. 17d). Also, the rapid strengthening of $(FLUX:T_{sfc})$ (Fig. 17d) and the similar correlation between FLUX and surface mixing ratio (not shown) indicates that storms with stronger oceanic heat fluxes begin to have warm, moist surface air over a large area surrounding their centers. With the weakening of downdrafts and enhanced FLUX easily overcoming their effects, convective instability near the center increases and provides a more favorable environment for strong convection (Fig. 17a). Thus, stronger storms are able to strengthen more quickly because they have stronger heat fluxes; this is the essence of the WISHE mechanism.

Figure 19 illustrates how the aforementioned factors lead to an increasingly large difference between the cyclones in member 1 (Fig. 19a-c) and member 19 (Fig. 19d-f) from 2100 UTC 12 September to 0300 UTC 13 September. Member 1 continues to have significant convection near the cyclone center, while most of the convection in member 19 is in a southwest to northeast oriented band well removed from the center. Likewise, the 2-km PV core is significantly better organized in member 1. As a result, the member-19 cyclone has significantly higher SLP and weaker surface winds (Fig. 11).

Finally, differences in landfall time after 0600 UTC have an effect on the ensemble that is dynamically similar to but increasingly more pronounced than the front. Because the front lies parallel to the coast, variance in frontal interaction must necessarily be associated with differences in the time that a storm is over water. While entrainment of post-frontal air certainly lowers instability and hinders convection, landfall is a much more severe instantaneous effect that completely shuts off the *source* of instability. The above correlation analysis was constructed in a way that minimizes the effects of landfall on the diagnosed dynamics (by using *SLPf* at 0600 UTC, before most members have made landfall) so that the above *other* factors could be investigated, but the landfall of storms thereafter leads to increasing spread until storms in most members have made landfall (see Fig. 3).

5.5 Deep-layer shear

Deep-layer shear is also known to inhibit genesis, so its relation to intensification in the ensembles is also briefly discussed here. Shear (computed as the vector difference between mean 200 and 850 hPa winds within 300 km of the center) before 1800 UTC is significantly correlated with *SLPf* (Fig. 5a), which indicates that either the initial shear is beneficial for

genesis or the pre-1800-UTC analysis increments do not correctly capture the relationship between upper level winds, convection, and storm intensity. Since ensemble-mean shear is quite low before 1800 UTC, it is possible that shear helps to organize convection during this time frame (e.g., as in Molinari et al. 2004), but determining the exact cause of this relationship is very difficult and beyond the scope of this paper. Nevertheless, after 1800 UTC shear intensifies and clearly becomes significantly anticorrelated with cyclone intensity.

6. Summary and Discussion

Using an EnKF-WRF analysis system and an ensemble forecast initialized with EnKF perturbations, this study has investigated the dynamics and predictability of Hurricane Humberto (2007). Humberto rapidly formed off the upper Texas coast and posed significant intensity forecast problems before its landfall less than a day later. Differences between ensemble members are utilized to expand upon the methodology of SZ08 to investigate why storms in some ensemble members rapidly form a hurricane and others do not.

There are multiple sources of the large intensity forecast spread observed in this study. Strength differences during the analysis period, before 1800 UTC 12 September, originate from differences in mid-level moisture and convective instability. Ensemble members with higher values of these parameters have more precipitation, which in turn results in stronger PV production. Spread in the CAPE analysis and forecast appears to be partly a result of differing positions of the front and the extent to which the front and cyclone interact. Therefore, uncertainty associated with the front introduces significant spread into the strength forecast. This

spread is later amplified by continued differences in CAPE and mid-level moisture, differences in the extent to which WISHE activates, and differing landfall times.

These results are significant because they generally confirm the findings of SZ08. Though the ensemble initialization method, the genesis environment, and the storm itself are very different here than in SZ08, MUCAPE and mid-level moisture have once again been found very important at determining how quickly cyclones initially strengthen in various ensemble members. The increase in spread due to WISHE is also similar to the findings of SZ08. Interestingly, the source of spread in the CAPE analysis and forecast here is different from that in SZ08, where higher MUCAPE was associated with stronger quasi-geostrophic lift. Thus, different mechanisms apparently can act to alter convective instability and consequently the rate at which cyclogenesis proceeds.

There are also significant differences between the current study and SZ08. First, while the role of MUCAPE was found to be secondary to that of mid-level moisture for intensification in SZ08, MUCAPE here appears to be at least as important of an intensification factor. This is probably due to the lower ensemble-mean MUCAPE and presence of the front in this case. With lower and more marginal instability for strong convection here, the addition of MUCAPE significantly affects the intensity and coverage of diabatic heating. In addition to the differing relative importance of MUCAPE and deep moisture, the areal extent of sensitivity to both thermodynamic fields is also very different here from SZ08. In SZ08 the correlation between $SLPf$ and both initial MUCAPE and mid-level moisture extended to the synoptic scale (not shown, but implied to some extent by the averaging area of the variables in that study), but in the current study the correlation is limited to mesoscale regions. For example, at 1500 UTC mid-

level moisture is correlated with precipitation (and *SLPf*) only in a band of southerly inflow, and MUCAPE is generally correlated to precipitation only in the convective inflow regions. This difference is very likely due to the difference in ensemble initialization and the presence of cold pools and mesoscale variations associated with the hot-start technique. A very similar pattern of (*MUCAPE:SLPf*) was seen (but not published) by 24 h in the background work for SZ08. This implies that, once mesoscale correlation structures became well established in SZ08, they were very similar to those observed here.

In general, the results herein demonstrate that there are cases when CAPE should be considered as a factor for tropical cyclone genesis. Yet, caution should be used when interpreting and applying this finding. Many cases have found that CAPE is not a factor (e.g., Nolan et al. 2007), or is at best generally a secondary factor (e.g., Cecil and Zipser 1999). This study does not take exception to those results, but rather it implies that there is a subset of systems – those for which CAPE is marginal to low – that can be quite sensitive to changes in CAPE. In certain circumstances, this could lead to poorer performance of prediction systems that do not use atmospheric instability as a predictor of genesis or intensification.

Ensemble spread in this situation was quite high, but improvements in analyses and model physics could likely reduce some of the uncertainty in this and other hurricane forecasts. For example, more numerous in situ observations can further refine the exact position of features such as fronts and better estimate the state of the atmosphere in regions that are currently only remotely sensed. A practical result of these improvements would be less ensemble spread later in the forecast period and more accurate representation of the true intensification by the ensemble mean.

Nevertheless, the behavior of the various ensemble members here and the results of ZS09 indicate that a certain (fairly large) degree of uncertainty might always be expected in some situations. For instance, the RMS spread of lower tropospheric variables in the 1800-UTC EnKF analysis is comparable to typical analysis error (not shown). Even if significant improvements were made to the analysis, it is likely that large (albeit less) strength spread would remain simply because of small differences in the trajectory of the cyclone and the time it would take for the cyclone to interact with both the front and land. Indeed, ZS09 found that error far smaller than can be detected by any analysis or observation system can determine whether or not a tropical cyclone will form. The very large spread in this case further demonstrates the limit of practical predictability of hurricane intensity discussed in ZS09 and illustrates the need for developing advanced ensemble prediction systems to provide event-dependent probabilistic forecasts and risk assessment.

Acknowledgements: This research started as part of the first author's doctoral dissertation at Texas A&M University. The authors have benefited from discussions with John Nielsen-Gammon, Scott Braun, and Larry Carey. Thanks are also due to Yonghui Weng for help on the ensemble simulations. This research is sponsored by the US Office of Naval Research under grants N000140410471 and N000140910526 and by NSF grant ATM-0840651.

REFERENCES

- Bei, N., and F. Zhang, 2007: Impacts of initial condition errors on mesoscale predictability of heavy precipitation along the Mei-Yu front in China. *Quart. J. Roy. Meteor. Soc.*, **133**, 83-99.
- Cecil, D. J., and E. J. Zipser, 1999, Relationships between tropical cyclone intensity and satellite-based indicators of inner core convection: 85-GHz ice-scattering signature and lightning. *Mon. Wea. Rev.*, **127**, 103-123.
- DeMaria, M., J. A. Knaff, and B. H. Connell, 2001: A tropical cyclone genesis parameter for the tropical Atlantic. *Wea. Forecasting*, **16**, 219-233.
- DeMaria, M., M. Mainelli, L. K. Shay, J. A. Knaff, and J. Kaplan, 2005: Further improvements to the Statistical Hurricane Intensity Prediction System (SHIPS). *Wea. Forecasting*, **20**, 531-543.
- Doswell, C. A. III, and E. N. Rasmussen, 1994: The effect of neglecting the virtual temperature correction on CAPE calculations. *Wea. Forecasting*, **9**, 625-629.
- Elsberry, R. L., T. D. B. Lambert, and M. A. Boothe, 2007: Accuracy of Atlantic and eastern North Pacific tropical cyclone intensity forecast guidance. *Wea. Forecasting*, **22**, 747-762.
- Emanuel, K. A., 1986: An air-sea interaction theory for tropical cyclones. Part I: Steady-state maintenance. *J. Atmos. Sci.*, **43**, 585-604.
- Emanuel, K. A., 1989: The finite-amplitude nature of tropical cyclogenesis. *J. Atmos. Sci.*, **46**, 3431-3456.
- Emanuel, K. A., J. D. Neelin, and C. S. Bretherton, 1994: On large scale circulations in convecting atmospheres. *Quart. J. Roy. Meteor. Soc.*, **120**, 1111-1144.
- Franklin, J. L., 2005: 2004 National Hurricane Center verification report. *Preprints*, 57th Interdepartmental Hurricane Conference, Miami, FL. [Updates are available on the official National Hurricane Center website: National Hurricane Center (NHC), www.nhc.noaa.gov/verification]
- Hakim, G. J., and R. D. Torn, 2008: Ensemble synoptic analysis. *Synoptic-Dynamic Meteorology and Weather Analysis and Forecasting: A Tribute to Fred Sanders*, Meteor. Monogr., Amer. Meteor. Soc., 440 pp.
- Hawblitzel, D. P., F. Zhang, Z. Meng, and C. A. Davis, 2007: Probabilistic evaluation of the dynamics and predictability of the mesoscale convective vortex of 10-13 June 2003. *Mon. Wea. Rev.*, **135**, 1544-1563.

- Haynes, P. H., and M. E. McIntyre, 1987: On the evolution of vorticity and potential vorticity in the presence of diabatic heating and frictional or other forces. *J. Atmos. Sci.*, **44**, 828–841.
- Hendricks, E. A., M. T. Montgomery, and C. A. Davis, 2004: The role of “vortical” hot towers in the formation of tropical cyclone Diana (1984). *J. Atmos. Sci.*, **61**, 1209–1232.
- Houze, R. A., S. S. Chen, B. F. Smull, W. C. Lee, and M. M. Bell, 2007: Hurricane intensity and eyewall replacement. *Science*, **315**, 1235–1238.
- Islam, S., R. L. Bras, and K. A. Emanuel, 1993: Predictability of mesoscale rainfalls in the tropics. *J. Appl. Meteor.*, **32**, 297–310.
- Kerns, B., and E. Zipser, 2009: Four years of tropical ERA-40 vorticity maxima tracks, Part II: Differences between developing and nondeveloping disturbances. *Mon. Wea. Rev.*, in press.
- Molinari, J., D. Vollaro, and K. L. Corbosiero, 2004: Tropical cyclone formation in a sheared environment: A case study. *J. Atmos. Sci.*, **61**, 2493–2509.
- Montgomery, M. T., M. E. Nichols, T. A. Cram, and A. Saunders, 2006: A vortical hot tower route to tropical cyclogenesis. *J. Atmos. Sci.*, **63**, 355–386.
- Nolan, D., E. D. Rappin, and K. A. Emanuel, 2007: Tropical cyclogenesis sensitivity to environmental parameters in radiative–convective equilibrium. *Quart. J. Roy. Meteor. Soc.*, **133**, 2085–2107.
- Olson, D. A., N. W. Junker, and B. Korty, 1995: Evaluation of 33 years of quantitative precipitation forecasting at the NMC. *Wea. Forecasting*, **10**, 498–511.
- Rotunno, R., and K. A. Emanuel, 1987: An air–sea interaction theory for tropical cyclones. Part II: Evolutionary study using a nonhydrostatic axisymmetric numerical model. *J. Atmos. Sci.*, **44**, 542–561.
- Sippel, J. A., J. W. Nielsen-Gammon, and S. E. Allen, 2006: The multiple-vortex nature of tropical cyclogenesis. *Mon. Wea. Rev.*, **134**, 1796–1814.
- Sippel, J. A., and F. Zhang, 2008: A probabilistic analysis of the dynamics and predictability of tropical cyclogenesis. *J. Atmos. Sci.*, **65**, 3440–3459.
- Van Sang, N., R. K. Smith, and M. T. Montgomery, 2008: Tropical-cyclone intensification and predictability in three dimensions. *Quart. J. Roy. Meteor. Soc.*, **134**, 563–582.
- Zhang, F., 2005: Dynamics and structure of mesoscale error covariance of a winter cyclone estimated through short-range ensemble forecasts. *Mon. Wea. Rev.*, **133**, 2876–2893.

Zhang, F., and J. A. Sippel, 2009: Effects of moist convection on hurricane predictability. *J. Atmos. Sci.*, in press.

Zhang, F., C. Snyder, and R. Rotunno, 2002: Mesoscale predictability of the “surprise” snowstorm of 24-25 January 2000. *Mon. Wea. Rev.*, **130**, 1617-1632.

Zhang, F., C. Snyder, and R. Rotunno, 2003: Effects of moist convection on mesoscale predictability. *J. Atmos. Sci.*, **60**, 1173-1185.

Zhang, F., A. M. Odins, and J. W. Nielsen-Gammon, 2006: Mesoscale Predictability of an Extreme Warm-Season Precipitation Event. *Wea. Forecasting*, **21**, 149-166.

Zhang, F., N. Bei, R. Rotunno, C. Snyder and C. C. Epifanio, 2007: Mesoscale predictability of moist baroclinic waves: Cloud-resolving experiments and multistage error growth dynamics. *J. Atmos. Sci.*, **64**, 3579-3594.

Zhang, F., Y. Weng, J. A. Sippel, Z. Meng, 2009, and C. H. Bishop: Cloud-resolving hurricane initialization and prediction through assimilation of Doppler radar observations with an ensemble Kalman filter: Humberto (2007). *Mon. Wea. Rev.*, in press.

LIST OF FIGURES

Figure 1. Radar reflectivity from (a) the KHGX WSR-88D radar and (b) the EnKF-analysis at 0900 UTC 12 September. Observed reflectivity in (a) is taken from the 0.5° elevation angle, and derived reflectivity in (b) is taken from the 2-km level. The two panels cover approximately the same domain, and reflectivity values are colored similarly in each panel. EnKF-analyzed surface wind vectors are shown in (b).

Figure 2. A scatterplot of SLP_t at 1800 UTC 12 September vs. SLP_f . The best-fit line is shown, and members 1, 16, and 19 are labeled and filled (these members are further analyzed in the text). The correlation coefficient is shown in the lower right corner.

Figure 3. The observed and ensemble forecast (a-b) intensity and (c-d) track of Hurricane Humberto. In panels (a) and (b) the best-track postanalysis intensity estimate (black) is compared with time evolution of (a) SLP and (b) wind from individual members of the EnKF analysis (green dashed) and subsequent ensemble forecast (green solid). In panel (c), tracks of all ensemble members (thin black or colored lines), the ensemble mean position (thick black solid line), and the best-track postanalysis (thick black dotted line) are plotted every 3-h from 1200 UTC 12 September to 1200 UTC 13 September. Panel (d) depicts the 0600 UTC 13 June forecast position with circles and tracks from select members with the 1800-UTC (final EnKF analysis) position noted by an 'x'. Color represents maximum intensity of the cyclone for the given member (black, $<25 \text{ m s}^{-1}$; blue $<30 \text{ m s}^{-1}$; green $<35 \text{ m s}^{-1}$; yellow $<40 \text{ m s}^{-1}$; red $>40 \text{ m s}^{-1}$). Before 1800 UTC, position is calculated from the EnKF analysis, and thereafter it is calculated from the ensemble forecast.

Figure 4. The 0900 UTC 12 September EnKF analysis of thermodynamic, height, PV, wind, and shear fields: (a) 700-hPa mixing ratio (filled every 1 g kg^{-1}), height (contoured every 10 m), and wind (full barb represents 5 m s^{-1}), (b) surface mixing ratio (filled every 1 g kg^{-1}), wind and SLP (contoured every 1 hPa), (c) surface temperature (contoured every 2 C), wind, and

MUCAPE (filled every 500 J kg⁻¹), and (d) 200-hPa height (contoured every 20 m), PV (smoothed, filled every 0.25 PVU for positive values and dash-contoured every 0.25 PVU for negative values), and 200-850-hPa shear (full barb represents 5 m s⁻¹).

Figure 5. The relationship between storm in intensity and (a) wind shear from 0900 UTC 12 September to 1200 UTC 13 September and (b) PV and precipitation from 0900 to 1800 UTC 12 September. In panel (a), wind shear (dotted) and the correlation between wind shear *SLPf* (solid) are shown. Wind shear is computed as the difference between the mean 200 and 850-hPa wind vectors averaged within 300 km of the circulation center. Until 1800 UTC, shear is calculated from the EnKF analysis, and after that time it is calculated from the ensemble forecast. Panel (b) shows the correlation between 2-km PV within the 2-PVU isopleth and *SLPf* (thick black), the correlation between *SLPf* and *PTOT* (thin black), the correlation between *PTOT* and *SLPf* when controlling for 2-km PV at the previous hour (thin dotted), and the correlation between *PTOT* and 2-km PV when controlling for 2-km PV at the previous hour (thick dotted). All variables are computed in a Lagrangian coordinate system following the storm center.

Figure 6. Radar reflectivity from (a) the KHGX WSR-88D radar and (b-d) the EnKF-analysis at the time of Humberto's observed and simulated landfall, respectively. Observed reflectivity in (a) is taken from the 0.5° elevation angle, and derived reflectivity in (b-d) is taken from the 2-km level in ensemble members (b) 1, (c) 16, and (d) 19. All panels cover approximately the same domain, and surface wind vectors and SLP (contoured every 5 hPa) are also shown, and the minimum central SLP is shown in the bottom left corner of each panel.

Figure 7. A mesoscale view of Humberto's landfall from both the (a) observed and (b) modeling perspectives. The analysis in (a) is from 0600 UTC 13 September and utilizes data from outside the displayed domain and at both earlier and later times for consistency. The central position and minimum pressure of the cyclone are determined from the NHC postanalysis valid at the same time. Full wind barbs represent 5 m s⁻¹ and analyzed fields are as follows: pressure is contoured every 5 hPa from 990 to 1005 hPa (thin black lines) and every 1 hPa at and

above 1010 hPa (thick black lines), and temperature is contoured every 1 C. The analysis in (b) is taken from member 1 of the ensemble at 1500 UTC 13 September. Surface temperature is shaded every 1 C, pressure is contoured as in (a), and surface wind vectors are shown.

Figure 8. RM-DTE (every 1 m s^{-1}) for the approximate area of domain 3 at (a) 1800 UTC 12 September and (b) 1200 UTC 13 September. Sampling is limited to every 7 grid points (31.5 km) in order to facilitate comparison with Fig. 5 from SZ08, which shows RM-DTE sampled to a 30-km grid.

Figure 9. Ensemble-mean 1-h precipitation (shaded every 5 mm), surface wind vectors, and 2-km PV (contoured at 2, 4, and 8 PVU) valid at 1000-1800 UTC 12 September. Analysis is completed in a Lagrangian coordinate system with the center of each panel at the ensemble mean center location. The region of PTOT, within the 10-mm isopleth, is outlined in black dots.

Figure 10. The evolution of surface winds vectors, 1-h precipitation (shaded every 5 mm) and PV (contoured at 2, 4, 8, and 16 PVU) for members (a-c) 1, (d-f) 16 and (g-i) 19 from 1600 to 1800 UTC 12 September.

Figure 11. Storm intensity in terms of (a) local and (b) area-average SLP (gray) and wind speed (black) for members 1 (thick solid), 10 (thick dotted), 16 (thin solid), and 19 (thin dotted). SLP is averaged within 20 km of the center, and surface winds are averaged within 60 km of the center.

Figure 12. Correlation between *PTOT* at the time indicated in each panel and MUCAPE two hours earlier. Correlation is contoured in solid (dashed) black at 0.3, 0.5, and 0.7 (-0.3, -0.5, -0.7) with increasing magnitude of correlation indicated by increasing line thickness. Ensemble-mean 1-h precipitation is shaded every 2.5 mm, and ensemble-mean surface wind vectors are shown.

Figure 13. The relationship between *PTOT16Z* and antecedent (a,d) *Tsfc*, (b,e) MUCAPE and (c,f) mid-level moisture in a Lagrangian, storm centered coordinate system. Ensemble-mean *Tsfc*, MUCAPE, and mid-level mixing ratio (average from 3-6 km) are respectively color filled at intervals of 1 K, 200 J kg⁻¹ and 0.5 g kg⁻¹ at (a-c) 1400 and (d-f) 1500 UTC 12 September. Correlation between the variable in each panel and *PTOT16Z* is contoured as in Fig. 12. Surface wind vectors are also shown in (a-b) and (d-e), and 3-6-km average wind vectors are shown in (c) and (f). The *PTOT16Z* region is contoured in white in panels (d-f), and the bold ‘X’ represents the position of the mean circulation center at 1600 UTC for reference.

Figure 14. Surface temperature (shaded every 1 K) and wind vectors for members (a) 1, (b) 16, and (c) 19 at 1400 UTC 12 September. The approximate leading edge of cool, post-frontal air (i.e., the 299-K isotherm) is marked with a bold dashed line.

Figure 15. Ensemble-mean Eulerian surface (a) temperature and (b) moisture fields as well as the correlation between *SLPf* and the respective fields at 0900 UTC 12 September. Temperature (moisture) is shaded every 1 K (1 g kg⁻¹), and correlation is contoured as in Fig. 12. The approximate location of the front is marked with the 298-K isotherm in (a) and the 17-g kg⁻¹ isodrosotherm in (b).

Figure 16. Surface mixing ratio (shaded every 1 g kg⁻¹) and wind vectors are shown for members (a) 1, (b) 16, and (c) 19 at 2100 UTC 12 September. The approximate leading edge of dry, post-frontal air is marked with a bold dashed line. The approximate leading edge of dry, post-frontal air is marked with a bold dashed line at the 17-g kg⁻¹ isodrosotherm.

Figure 17. The Lagrangian evolution of (a) ensemble-mean MUCAPE (shaded every 100 J kg⁻¹) and its correlation with *SLPf* controlled for *SLPt*, (b) ensemble-mean mid-level (3-6-km average) moisture (shaded every 0.5 g kg⁻¹) and its correlation with *SLPf* controlled for *SLPt*, (c) ensemble-mean diabatic heating averaged over 1-9 km (*DH*, shaded every 0.5 K h⁻¹) and its correlation with *SLPf*, and (d) ensemble-mean total heat fluxes (*FLUX*, shaded every 100

W m^{-2}) overlain with (*FLUX:SLPf*) (black), and (*FLUX:Tsf_c*) (white) as a function of radius and time. All variables are displayed as a function of radius and time, and *DH*, *Tsf_c*, and moisture are averaged in 20-km annuli before the correlation is computed. Correlation is contoured as in Fig. 12.

Figure 18. Ensemble-mean precipitation (shaded every 10 mm) from (a) 1800 to 2100 UTC, (b) 2100 to 0000 UTC, and (c) 0000 to 0300 UTC and correlation between *Tsf_c* and area-average precipitation within the gray box. Correlation is contoured as in Fig. 12, and surface wind vectors are also shown. Analysis is completed in a Lagrangian coordinate system with the center of each panel at the ensemble mean center location.

Figure 19. The evolution of PV (contoured at every 5 PVU with increasing thickness indicating increasing values) and simulated radar reflectivity (shaded every 10 dBZ) for members (a-c) 1 and (j-m) 19.

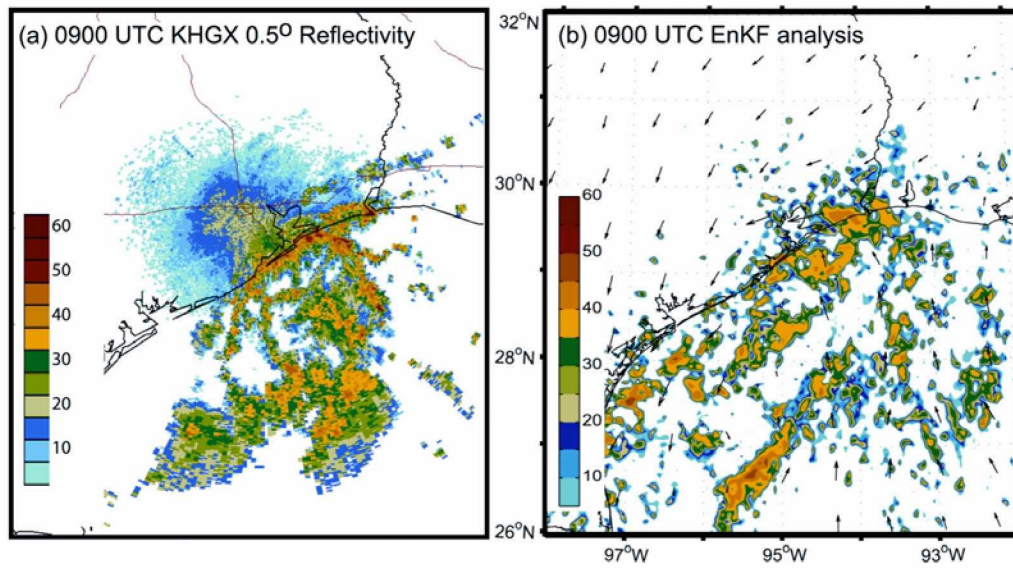


Figure 1. Radar reflectivity from (a) the KHGX WSR-88D radar and (b) the EnKF-analysis at 0900 UTC 12 September. Observed reflectivity in (a) is taken from the 0.5° elevation angle, and derived reflectivity in (b) is taken from the 2-km level. The two panels cover approximately the same domain, and reflectivity values are colored similarly in each panel. EnKF-analyzed surface wind vectors are shown in (b).

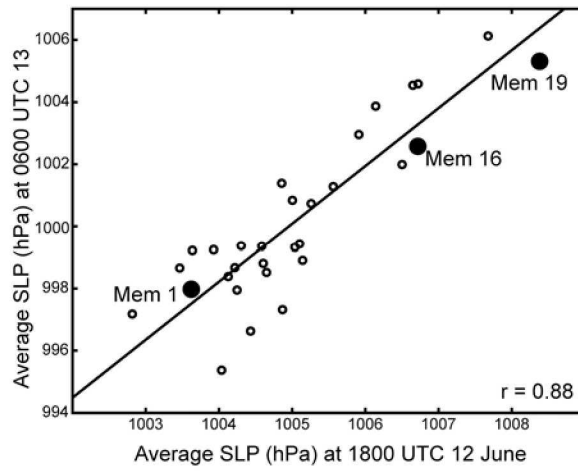


Figure 2. A scatterplot of *SLP_t* at 1800 UTC 12 September vs. *SLP_f*. The best-fit line is shown, and members 1, 16, and 19 are labeled and filled (these members are further analyzed in the text). The correlation coefficient is shown in the lower right corner.

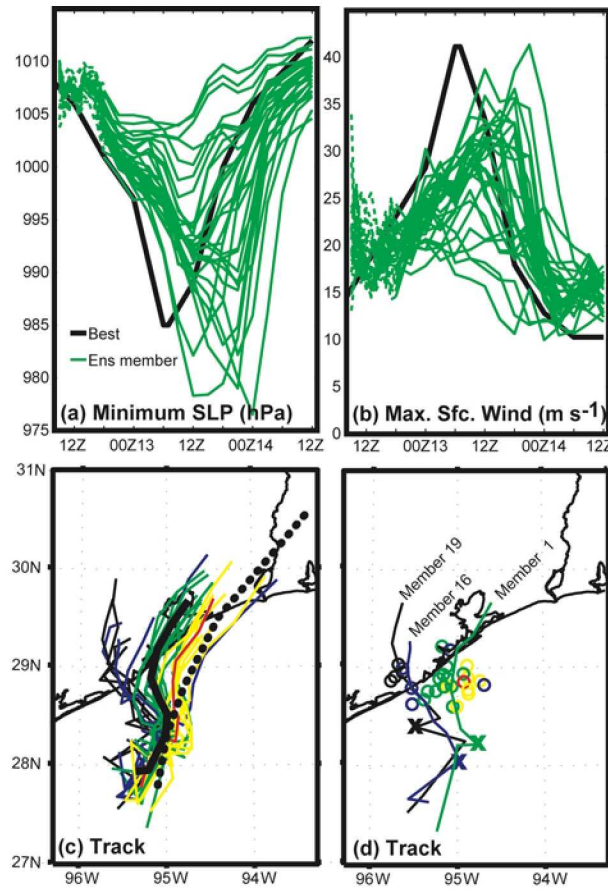


Figure 3. The observed and ensemble forecast (a-b) intensity and (c-d) track of Hurricane Humberto. In panels (a) and (b) the best-track postanalysis intensity estimate (black) is compared with time evolution of (a) SLP and (b) wind from individual members of the EnKF analysis (green dashed) and subsequent ensemble forecast (green solid). In panel (c), tracks of all ensemble members (thin black or colored lines), the ensemble mean position (thick black solid line), and the best-track postanalysis (thick black dotted line) are plotted every 3-h from 1200 UTC 12 September to 1200 UTC 13 September. Panel (d) depicts the 0600 UTC 13 June forecast position with circles and tracks from select members with the 1800-UTC (final EnKF analysis) position noted by an 'x'. Color represents maximum intensity of the cyclone for the given member (black, <25 m s⁻¹; blue <30 m s⁻¹; green <35 m s⁻¹; yellow <40 m s⁻¹; red >40 m s⁻¹). Before 1800 UTC, position is calculated from the EnKF analysis, and thereafter it is calculated from the ensemble forecast.

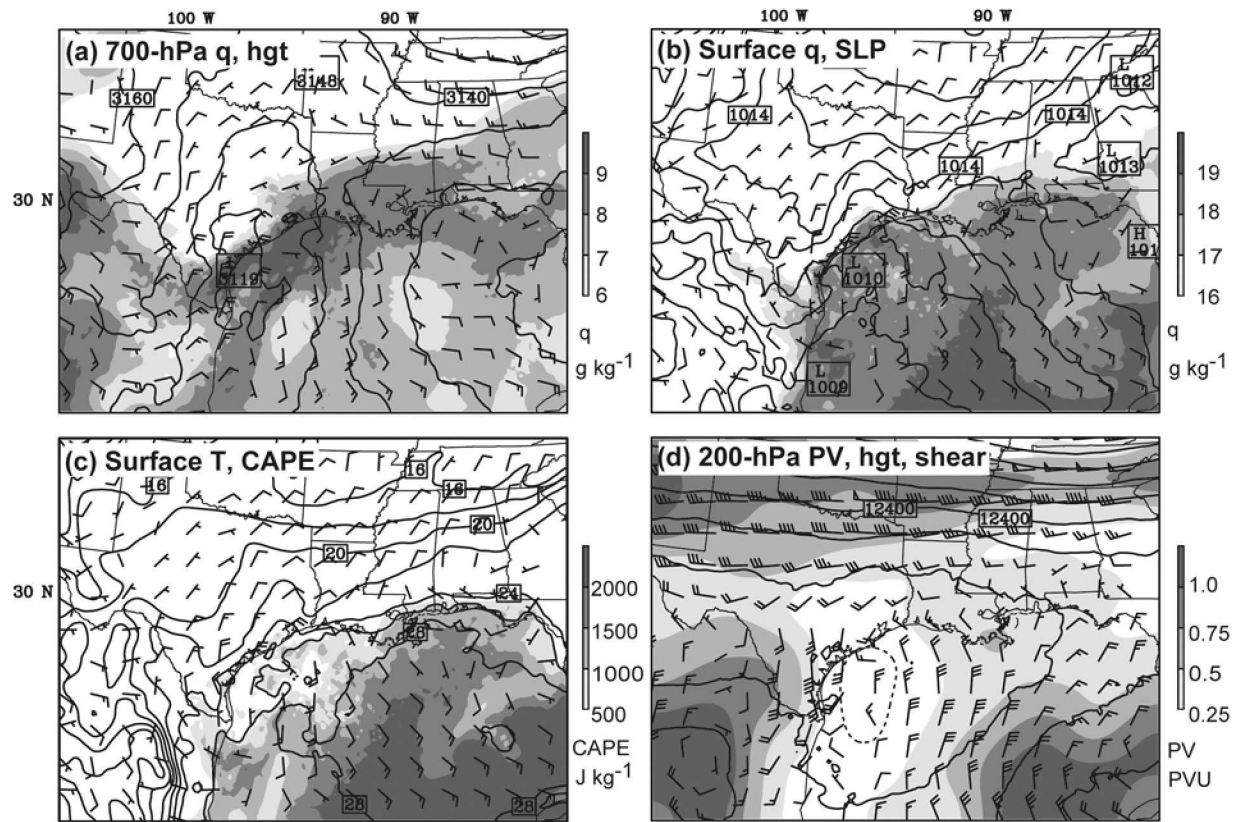


Figure 4. The 0900 UTC 12 September EnKF analysis of thermodynamic, height, PV, wind, and shear fields: (a) 700-hPa mixing ratio (filled every 1 g kg⁻¹), height (contoured every 10 m), and wind (full barb represents 5 m s⁻¹), (b) surface mixing ratio (filled every 1 g kg⁻¹), wind and SLP (contoured every 1 hPa), (c) surface temperature (contoured every 2 C), wind, and MUCAPE (filled every 500 J kg⁻¹), and (d) 200-hPa height (contoured every 20 m), PV (smoothed, filled every 0.25 PVU for positive values and dash-contoured every 0.25 PVU for negative values), and 200-850-hPa shear (full barb represents 5 m s⁻¹)

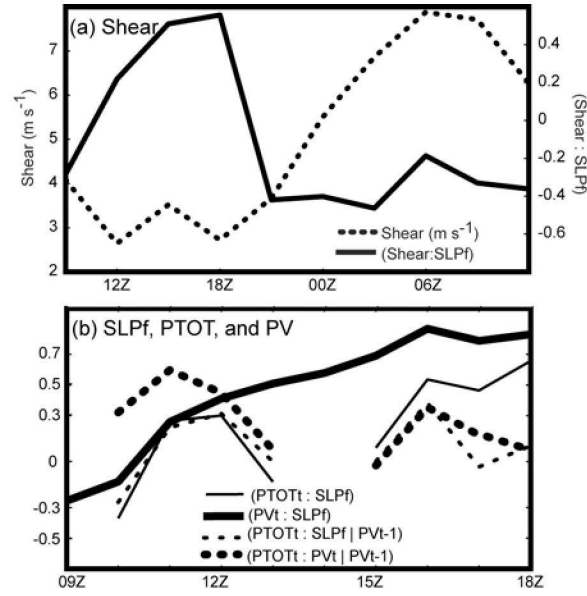


Figure 5. The relationship between storm in intensity and (a) wind shear from 0900 UTC 12 September to 1200 UTC 13 September and (b) PV and precipitation from 0900 to 1800 UTC 12 September. In panel (a), wind shear (dotted) and the correlation between wind shear $SLPf$ (solid) are shown. Wind shear is computed as the difference between the mean 200 and 850-hPa wind vectors averaged within 300 km of the circulation center. Until 1800 UTC, shear is calculated from the EnKF analysis, and after that time it is calculated from the ensemble forecast. Panel (b) shows the correlation between 2-km PV within the 2-PVU isopleth and $SLPf$ (thick black), the correlation between $SLPf$ and $PTOT$ (thin black), the correlation between $PTOT$ and $SLPf$ when controlling for 2-km PV at the previous hour (thin dotted), and the correlation between $PTOT$ and 2-km PV when controlling for 2-km PV at the previous hour (thick dotted). All variables are computed in a Lagrangian coordinate system following the storm center.

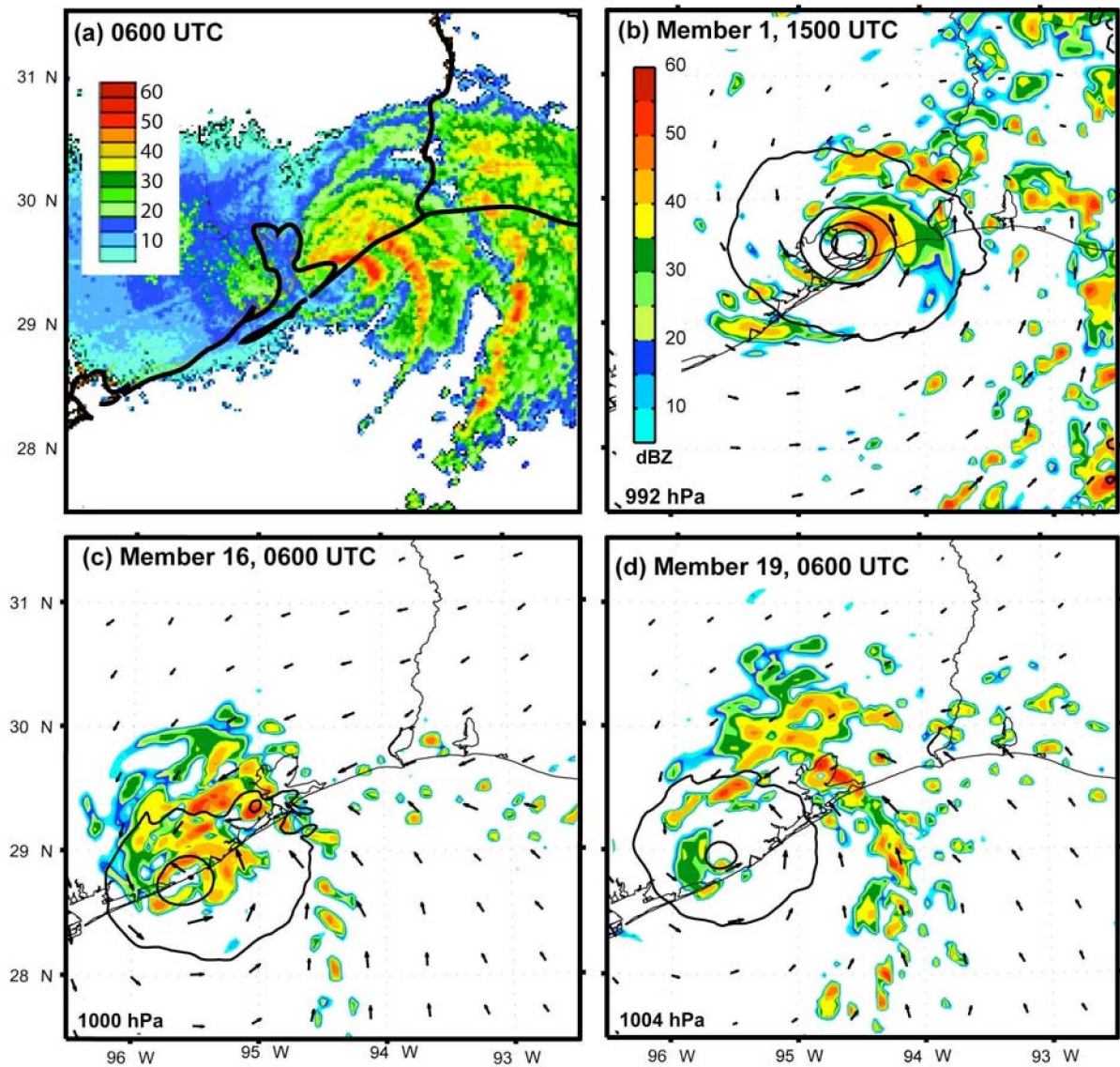


Figure 6. Radar reflectivity from (a) the KHGX WSR-88D radar and (b-d) the EnKF-analysis at the time of Humberto's observed and simulated landfall, respectively. Observed reflectivity in (a) is taken from the 0.5° elevation angle, and derived reflectivity in (b-d) is taken from the 2-km level in ensemble members (b) 1, (c) 16, and (d) 19. All panels cover approximately the same domain, and surface wind vectors and SLP (contoured every 5 hPa) are also shown, and the minimum central SLP is shown in the bottom left corner of each panel.

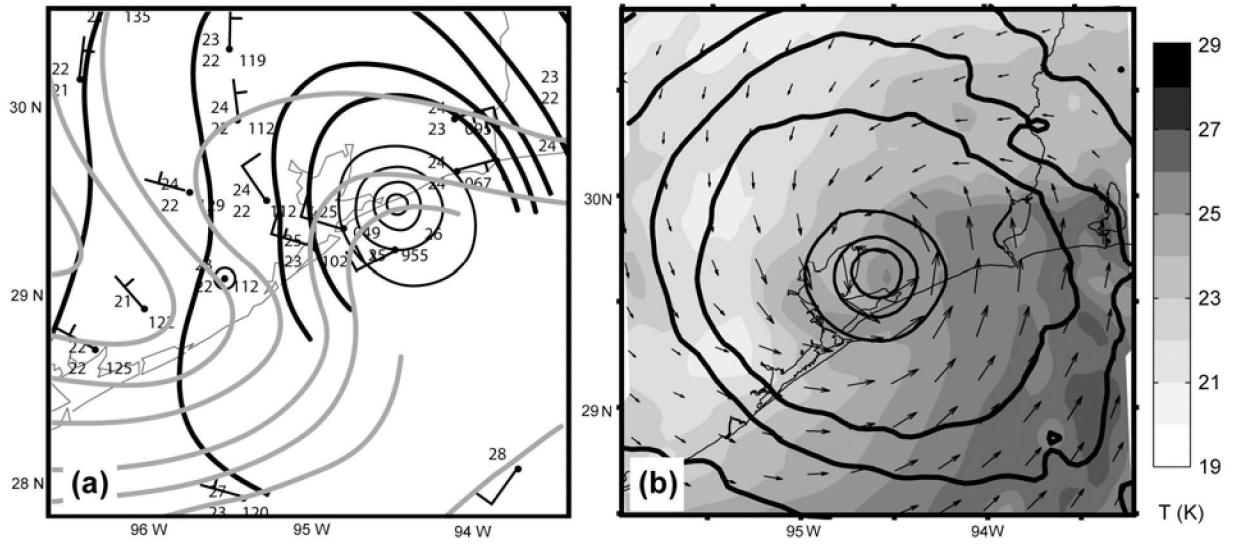


Figure 7. A mesoscale view of Humberto's landfall from both the (a) observed and (b) modeling perspectives. The analysis in (a) is from 0600 UTC 13 September and utilizes data from outside the displayed domain and at both earlier and later times for consistency. The central position and minimum pressure of the cyclone are determined from the NHC postanalysis valid at the same time. Full wind barbs represent 5 m s^{-1} and analyzed fields are as follows: pressure is contoured every 5 hPa from 990 to 1005 hPa (thin black lines) and every 1 hPa at and above 1010 hPa (thick black lines), and temperature is contoured every 1 C. The analysis in (b) is taken from member 1 of the ensemble at 1500 UTC 13 September. Surface temperature is shaded every 1 C, pressure is contoured as in (a), and surface wind vectors are shown.

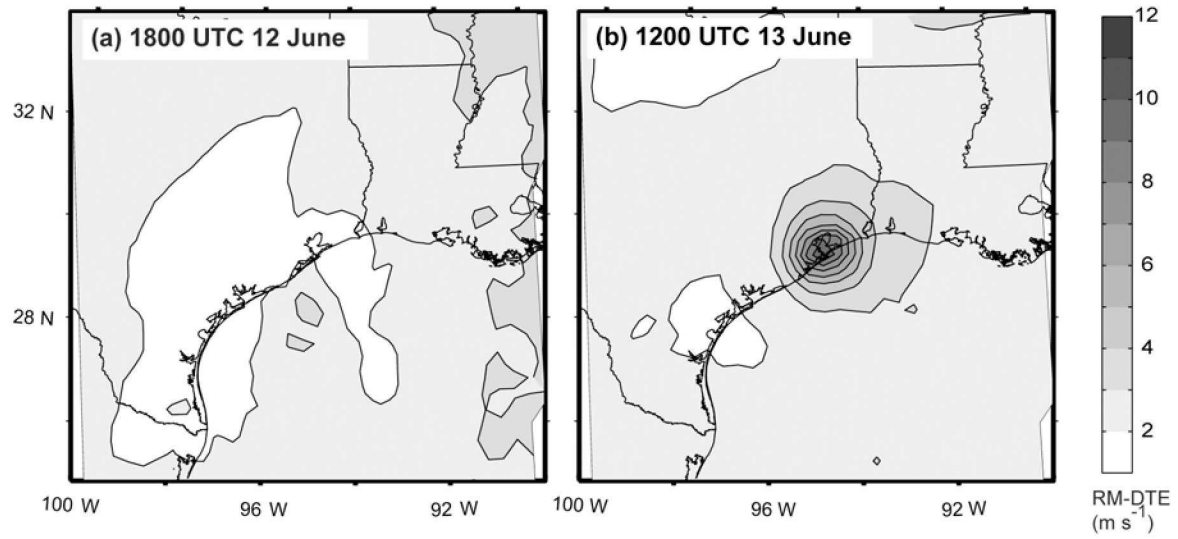


Figure 8. RM-DTE (every 1 m s^{-1}) for the approximate area of domain 3 at (a) 1800 UTC 12 September and (b) 1200 UTC 13 September. Sampling is limited to every 7 grid points (31.5 km) in order to facilitate comparison with Fig. 5 from SZ08, which shows RM-DTE sampled to a 30-km grid.

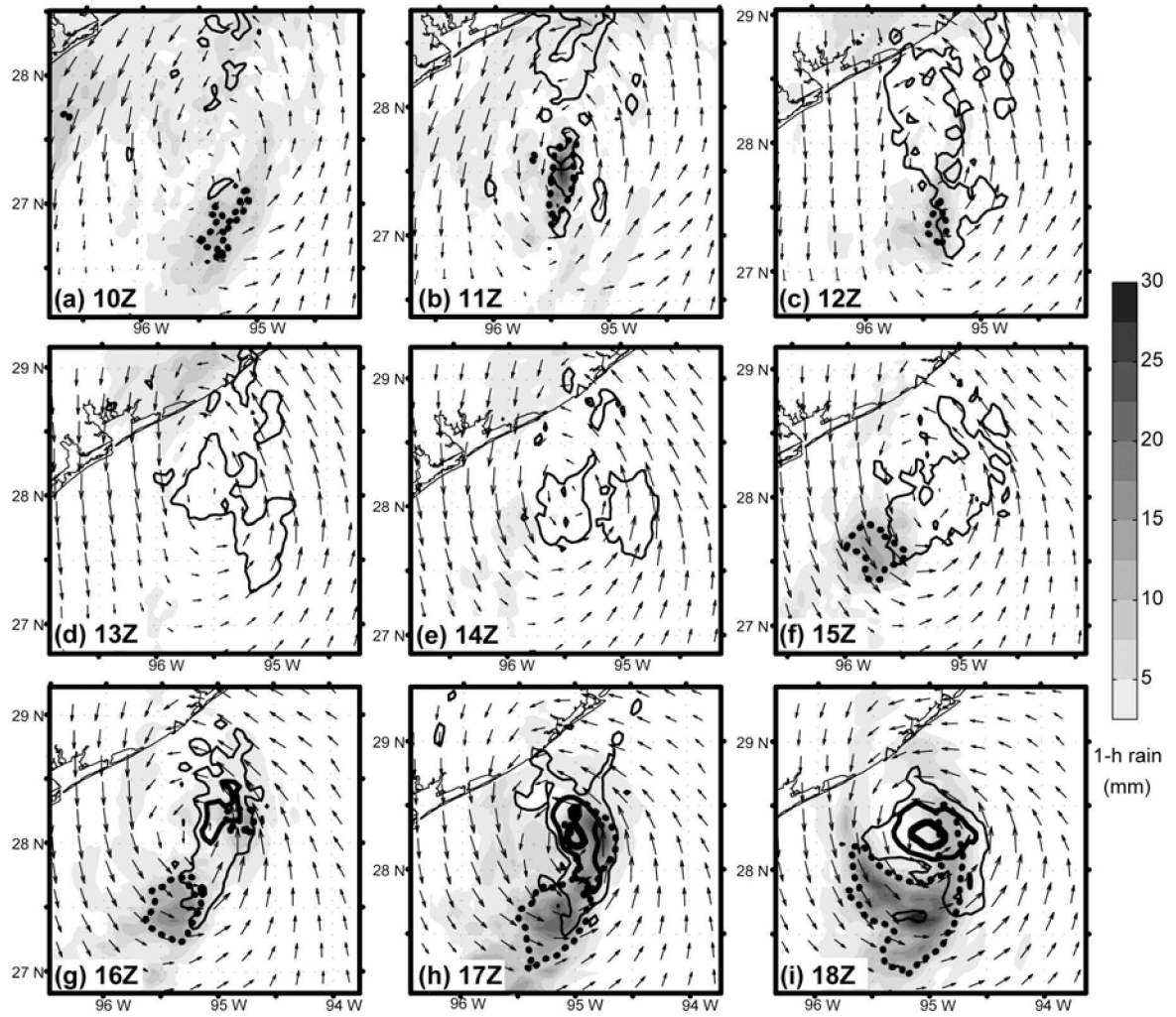


Figure 9. Ensemble-mean 1-h precipitation (shaded every 5 mm), surface wind vectors, and 2-km PV (contoured at 2, 4, and 8 PVU) valid at 1000-1800 UTC 12 September. Analysis is completed in a Lagrangian coordinate system with the center of each panel at the ensemble mean center location. The region of PTOT, within the 10-mm isopleth, is outlined with black dots.

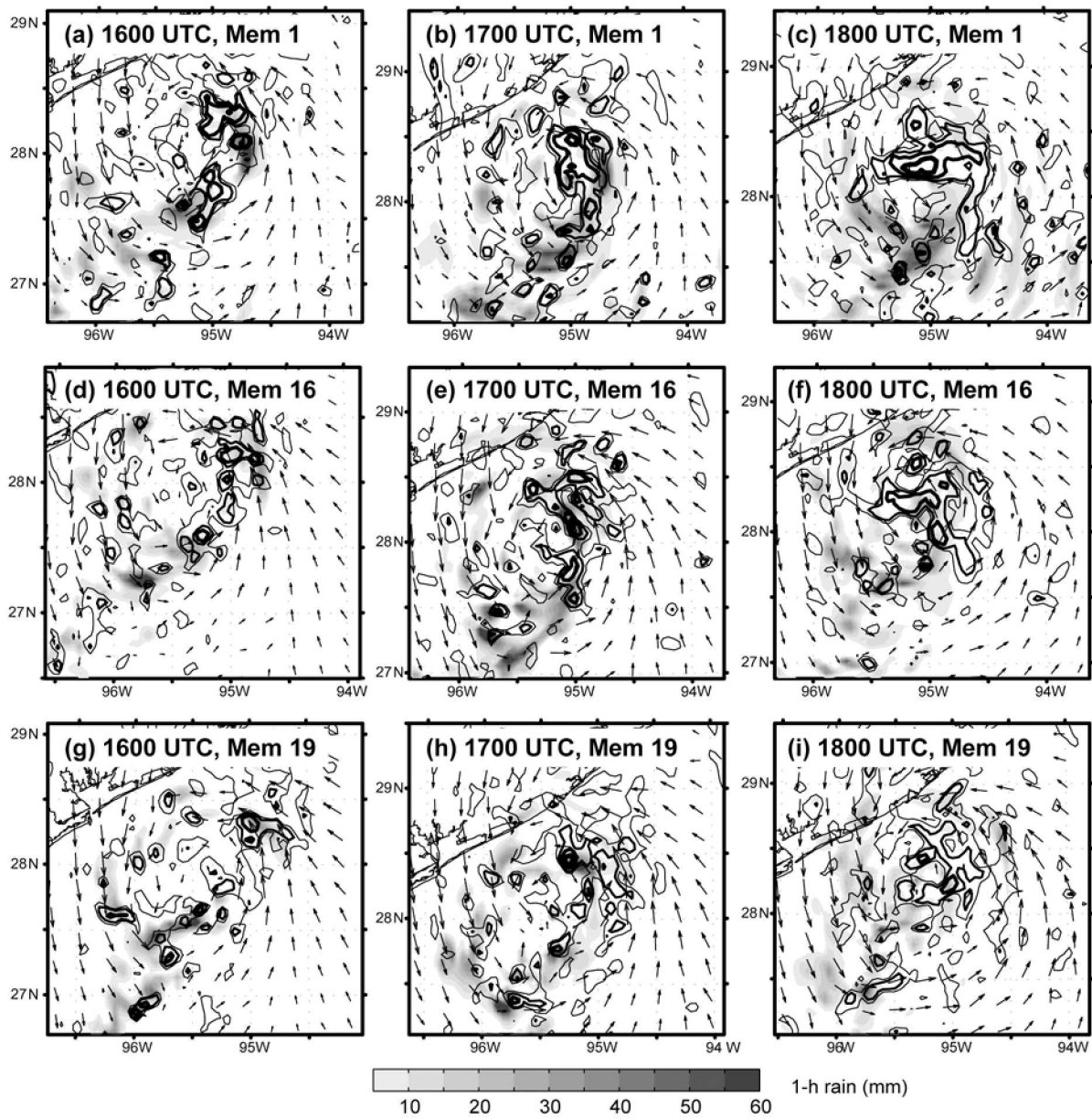


Figure 10. The evolution of surface winds vectors, 1-h precipitation (shaded every 5 mm) and PV (contoured at 2, 4, 8, and 16 PVU) for members (a-c) 1, (d-f) 16 and (g-i) 19 from 1600 to 1800 UTC 12 September.

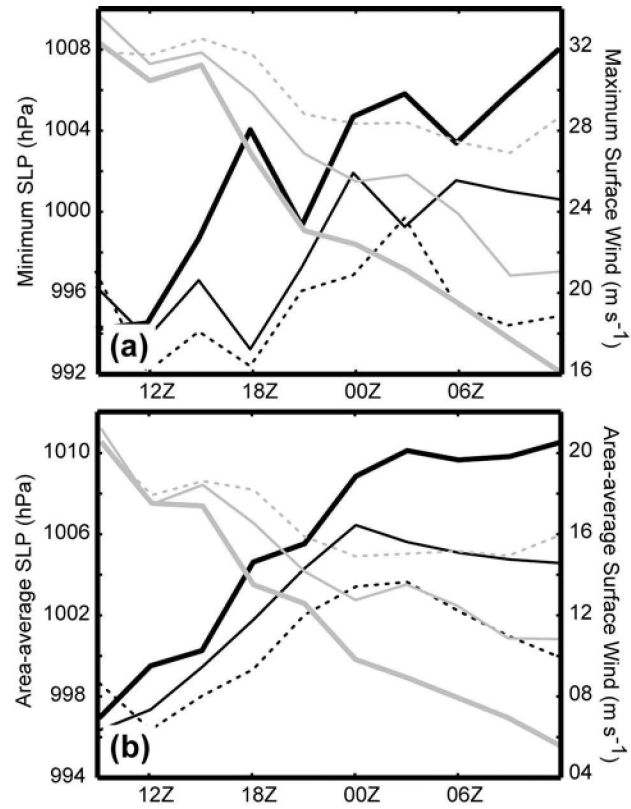


Figure 11. Storm intensity in terms of (a) local and (b) area-average SLP (gray) and wind speed (black) for members 1 (thick solid), 10 (thick dotted), 16 (thin solid), and 19 (thin dotted). SLP is averaged within 20 km of the center, and surface winds are averaged within 60 km of the center.

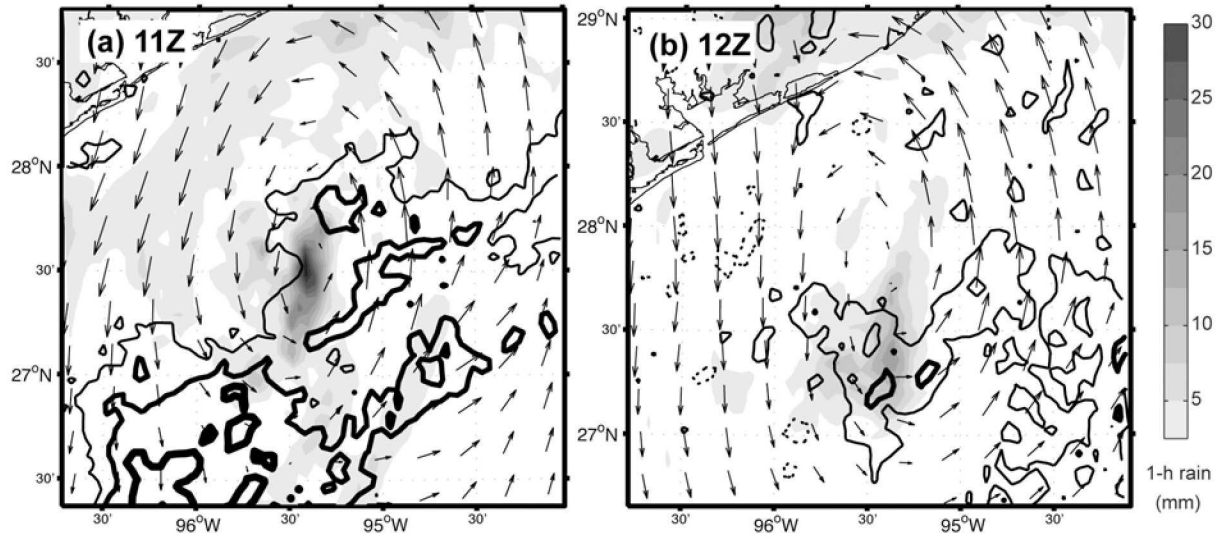


Figure 12. Correlation between PTOT at the time indicated in each panel and MUCAPE two hours earlier. Correlation is contoured in solid (dashed) black at 0.3, 0.5, and 0.7 (-0.3, -0.5, -0.7) with increasing magnitude of correlation indicated by increasing line thickness. Ensemble-mean 1-h precipitation is shaded every 2.5 mm, and ensemble-mean surface wind vectors are shown.

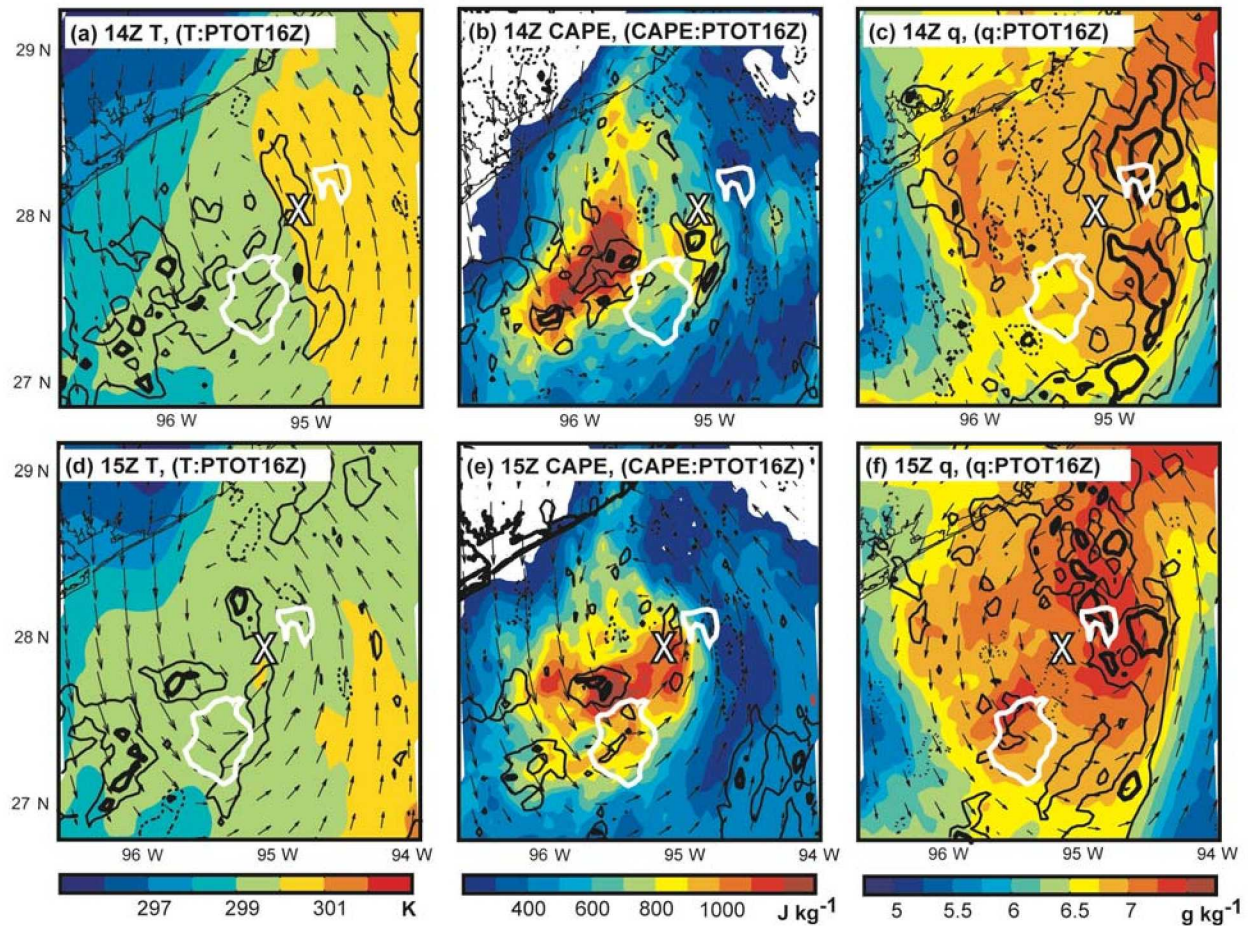


Figure 13. The relationship between *PTOT16Z* and antecedent (a,d) *Tsfc*, (b,e) MUCAPE and (c,f) mid-level moisture in a Lagrangian, storm centered coordinate system. Ensemble-mean *Tsfc*, MUCAPE, and mid-level mixing ratio (average from 3–6 km) are respectively color filled at intervals of 1 K, 200 J kg⁻¹, 0.5 g kg⁻¹ at (a-c) 1400 and (d-f) 1500 UTC 12 September. Correlation between the variable in each panel and *PTOT16Z* is contoured as in Fig. 12. Surface wind vectors are shown in (a-b) and (d-e), and 3–6-km average wind vectors are shown in (c) and (f). The *PTOT16Z* region is contoured in white, and the bold ‘X’ represents the position of the mean circulation center at 1600 UTC for reference.

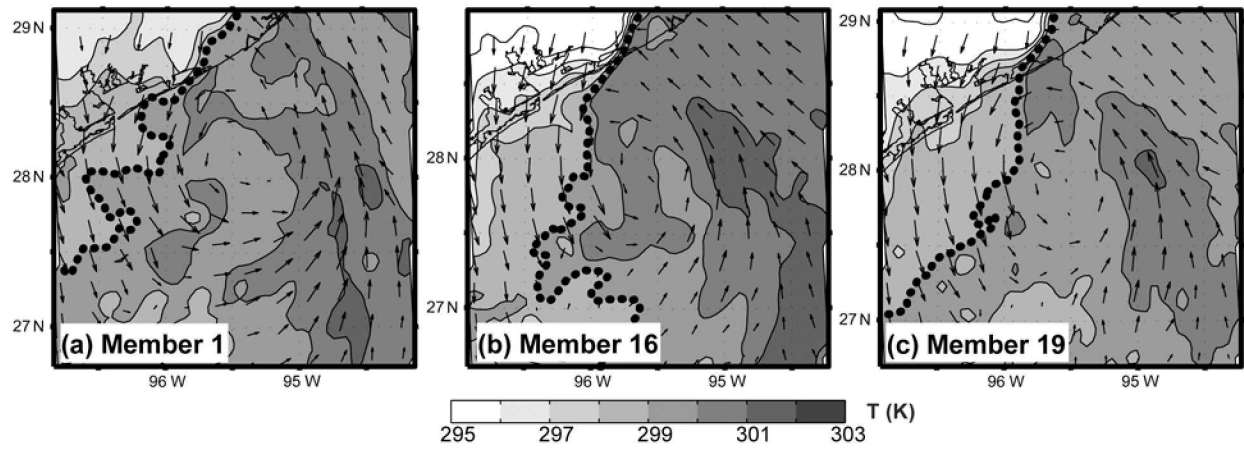


Figure 14. Surface temperature (shaded every 1 K) and wind vectors for members (a) 1, (b) 16, and (c) 19 at 1400 UTC 12 September. The approximate leading edge of cool, post-frontal air (i.e., the 299-K isotherm) is marked with a bold dashed line.

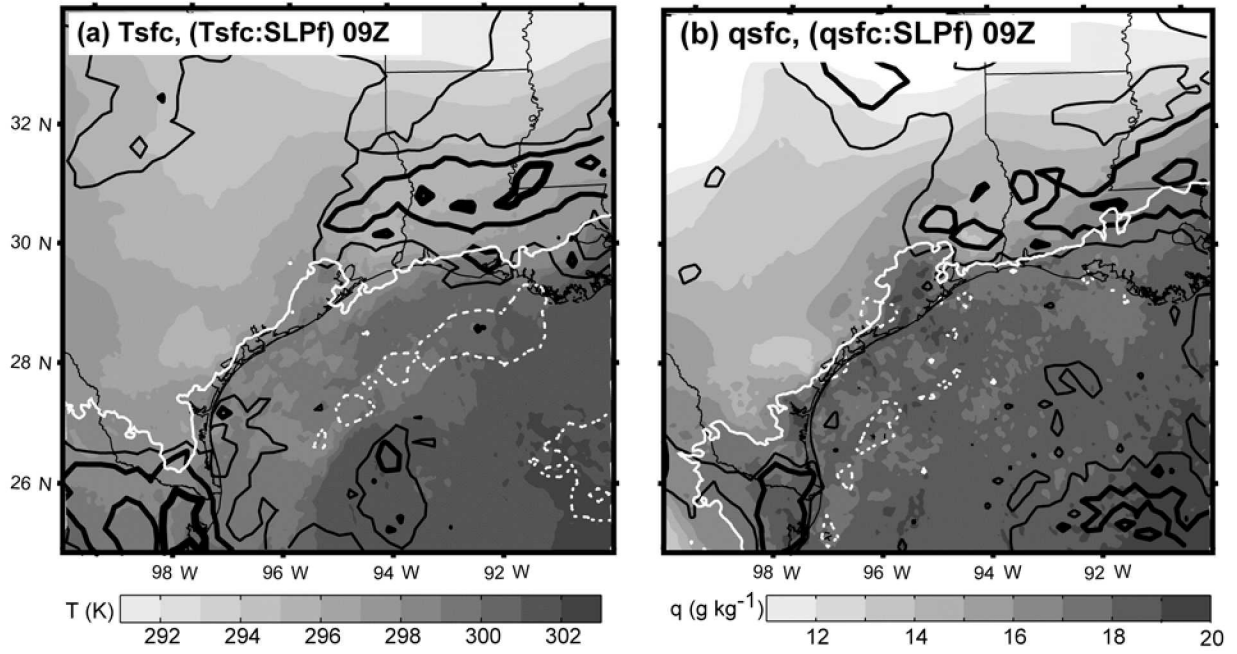


Figure 15. Ensemble-mean Eulerian surface (a) temperature and (b) moisture fields as well as the correlation between $SLPf$ and the respective fields at 0900 UTC 12 September. Temperature (moisture) is shaded every 1 K (1 g/kg), and correlation is contoured as in Fig. 12. The approximate location of the front is marked with the 298-K isotherm in (a) and the 17- g/kg isodrosotherm in (b).

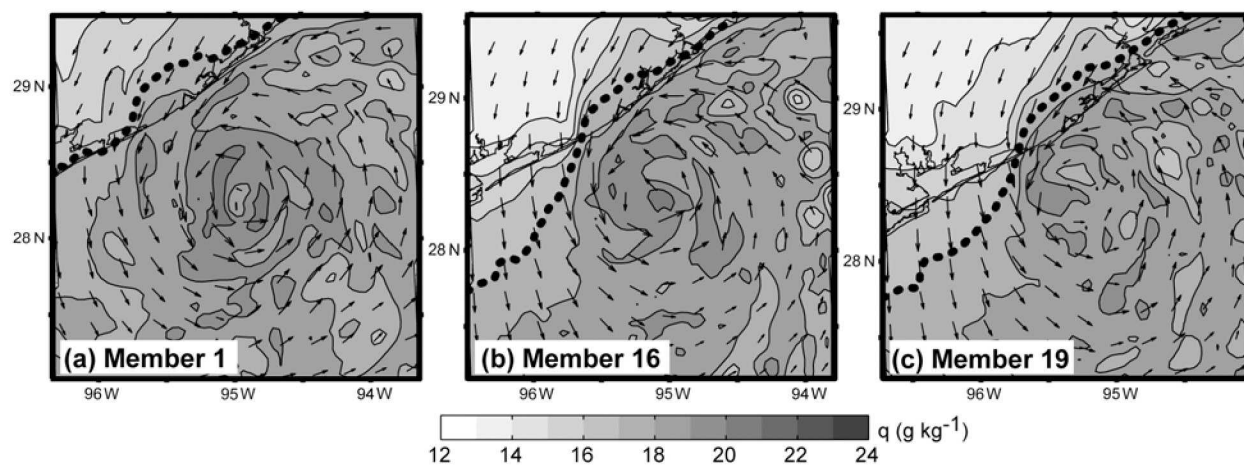


Figure 16. Surface mixing ratio (shaded every 1 g/kg) and wind vectors are shown for members (a) 1, (b) 16, and (c) 19 at 2100 UTC 12 September. The approximate leading edge of dry, post-frontal air is marked with a bold dashed line at the 17-g/kg isodrosotherm.

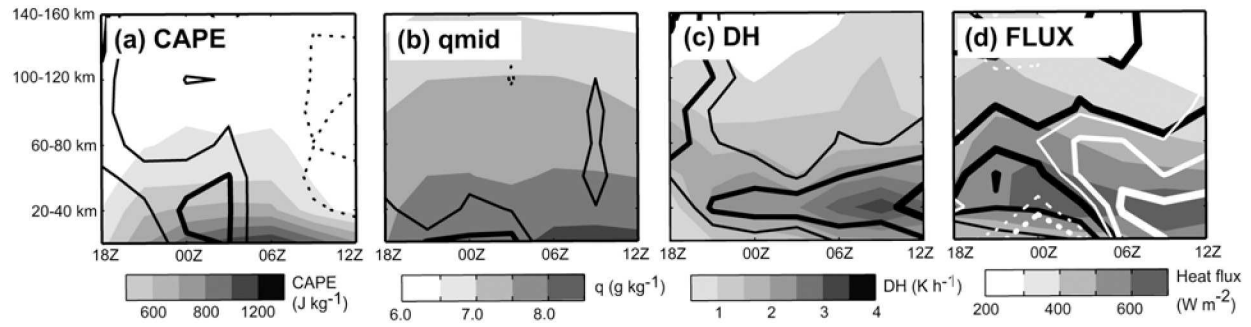


Figure 17. The Lagrangian evolution of (a) ensemble-mean MUCAPE (shaded every 100 J/kg) and its correlation with $SLPf$ controlled for $SLPt$, (b) ensemble-mean mid-level (3-6-km average) moisture (shaded every 0.5 g kg⁻¹) and its correlation with $SLPf$ controlled for $SLPt$, (c) ensemble-mean diabatic heating averaged over 1-9 km (DH , shaded every 0.5 K h⁻¹) and its correlation with $SLPf$, and (d) ensemble-mean total heat fluxes ($FLUX$, shaded every 100 W m⁻²) overlain with ($FLUX:SLPf$) (black), and ($FLUX:Tsfc$) (white) as a function of radius and time. All variables are displayed as a function of radius and time, and DH , $Tsfc$, and moisture are averaged in 20-km annuli before the correlation is computed. Correlation is contoured as in Fig. 12.

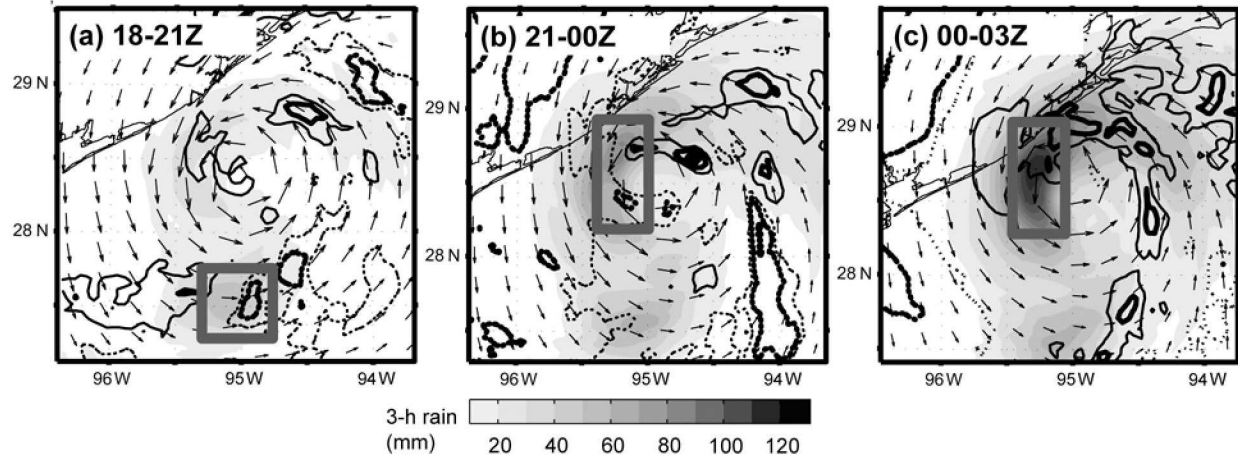


Figure 18. Ensemble-mean precipitation (shaded every 10 mm) from (a) 1800 to 2100 UTC, (b) 2100 to 0000 UTC, and (c) 0000 to 0300 UTC and correlation between $Tsfc$ and area-average precipitation within the gray box. Correlation is contoured as in Fig. 12, and surface wind vectors are also shown. Analysis is completed in a Lagrangian coordinate system with the center of each panel at the ensemble mean center location.

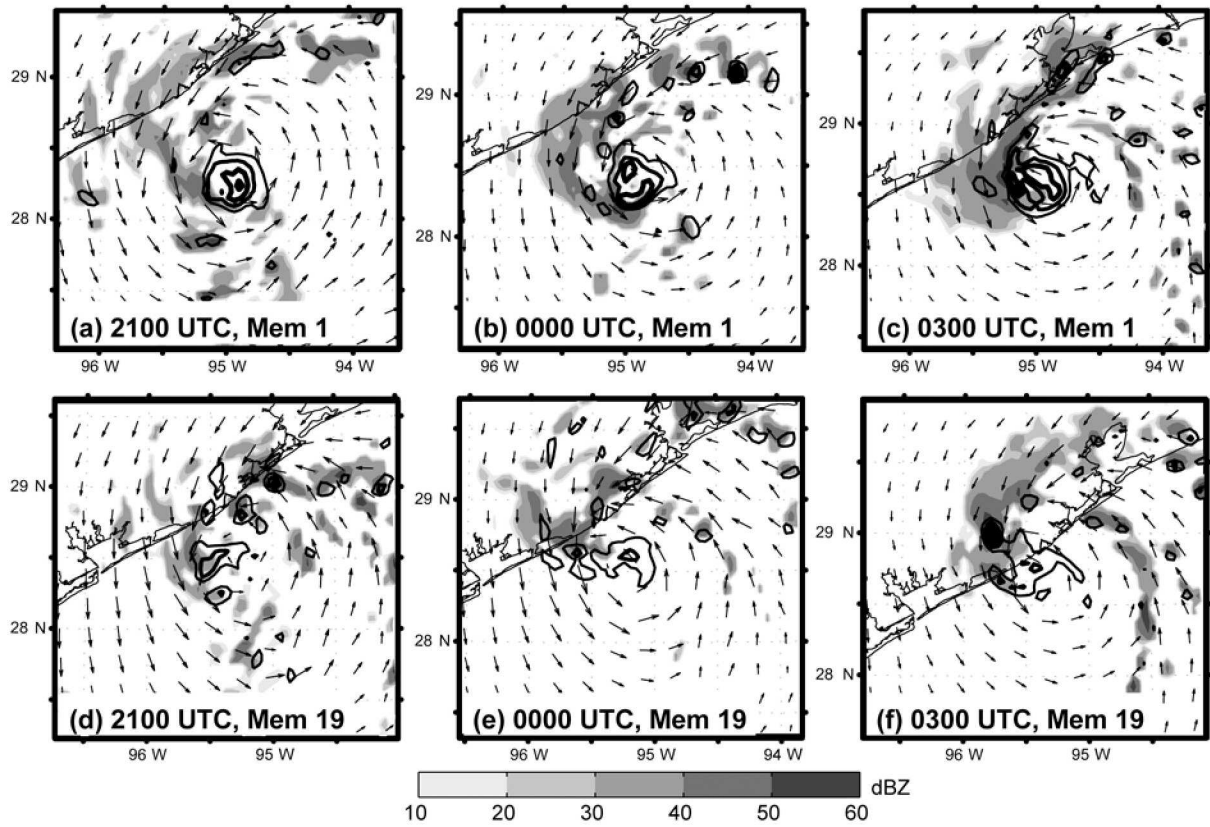


Figure 19. The evolution of PV (contoured at every 5 PVU with increasing thickness indicating increasing values) and simulated radar reflectivity (shaded every 10 dBZ) for members (a-c) 1 and (j-m) 19.

Popular summary for:

Dynamics and Predictability of Hurricane Humberto (2007)
Revealed from Ensemble Analysis and Forecasting

By:

Jason A. Sippel and Fuqing Zhang

Submitted to: Journal of Atmospheric Sciences

This study uses short-range ensemble forecasts initialized with radar velocity data in an Ensemble-Kalman filter to study Hurricane Humberto, which made landfall along the Texas coast in 2007. Statistical correlation is used to determine why some ensemble members strengthen the incipient low into a hurricane and others do not. It is found that deep moisture and high convective available potential energy (CAPE) are two of the most important factors for the genesis of Humberto. CAPE differences here are related to the interaction between the cyclone and a nearby front, which tends to stabilize the lower troposphere in the vicinity of the circulation center. This subsequently weakens convection and slows genesis. Eventually the wind-induced surface heat exchange mechanism and differences in landfall time result in even larger ensemble spread.